

FIG. 1. Schematic figure of the beam line for this experiment.

In contrast to the technical progress made with our irradiation system, there has been little investigation of the biological response of human cells to high dose rate protons. The relative biological effectiveness (RBE) is one of the most commonly used parameters for characterizing the biological effectiveness of proton beams. Until now, we have been using the same RBE of 1.1 for all doses, dose rates, and linear energy transfers (LETs). This value is in good agreement with that previously measured at spread-out Bragg peak (SOBP) center for SCC61 human squamous cell carcinoma, NB1RGB human fibroblasts, V79 Chinese hamster cells,⁶ and human salivary gland (HSG) tumor-originating cells⁷ at a dose rate of 1.6–2.7 Gy/min. However, it is not yet clear whether this value could be applied to high dose rate proton therapy. There have been a number of reports on the RBE in ultrahigh dose rate (UDR) regimes using protons provided by tandem accelerator (10^3 – 10^4 Gy/min for their continuous mode),^{8,9} pulse x rays from laser-produced plasma,¹⁰ electron pulse,¹¹ and the comprehensive literature review about the dose rate effects was done.¹² The former study used protons; however, it was limited to a 3 Gy dose and therefore, no overall survival curve was drawn. The LET dependence of the dose rate effect was also not investigated.

The aim of this study is to clarify whether the biological effectiveness of a high dose rate proton beam is different from that of the present dose rate. Since the LET of protons varies according to the depth of the patient's body being irradiated, data were obtained at multiple LETs. The experiment was performed using HSG cells *in vitro* and the surviving fraction (SF) was determined by a clonogenic assay.

II. MATERIALS AND METHODS

II.A. Beamline and experimental setup

In this experiment, we used the nozzle designed for the dual-ring double scattering method^{13,14} in order to obtain flat dose profile and stable dose intensity over the cell containing area. A 235 MeV proton beam produced by an AVF cyclotron was scattered using two thin scatterers on the beamline. These scatterers made it possible to obtain a flat dose profile over the cell containing area ($\pm 2.5\%$ over 2×5 cm² field). The beam was then cut off using a 15 cm \times 15 cm collimator. The experimental setup is shown in Fig. 1.

The HSG cells were placed in the bottom of a slide chamber flask (Lab-Tech SlideFlask 170920, Nunc, Chicago, IL). The flask was then placed in a polyethylene block (0.98 g/cm³) containing a specially designed space for the

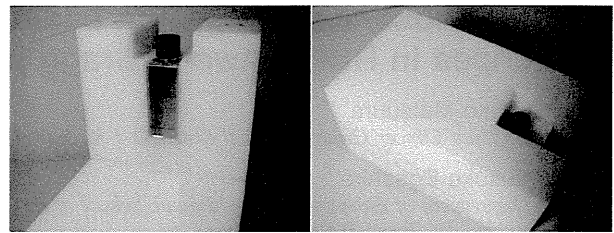


FIG. 2. The flask was placed in a specially molded polyethylene block (0.98 g/cm³) containing a space to hold it. The thicknesses of the polyethylene block in front of the flask were chosen so that the cells were located at the Bragg peak and plateau, respectively.

flask (Fig. 2). The surface of the cells was placed at the isocenter of the proton beam. In order to obtain the highest dose rate in this setup, as well as to investigate the LET dependence, the flask was placed at the Bragg peak and the plateau of the Bragg curve by placing polyethylene blocks of appropriate thickness in front of the flask. Figure 3 shows the measured/simulated distal dose profile and the LET distribution $f(L_D)$ at the flask positions used in this experiment. The simulation was performed using a GEANT4 toolkit (ver. 4.9.2) and PTSGEOM.¹⁵ Under these conditions, the absorbed dose-averaged LET (\bar{L}_D) at the Bragg peak and plateau were 3.19 keV/ μ m (equivalent to an energy of 15.8 MeV) and 0.56 keV/ μ m (equivalent to an energy of 146 MeV), respectively.¹⁶

II.B. Method for calibrating the dose and dose rate

The measurement of the dose and dose rate was conducted with PTW Markus Chambers (Type 23343; PTW, Freiburg, Germany) and an electrometer (FLUKE35040; Fluke Biomedical, Cleveland, OH). Then GafChromic EBT film (International Specialty Products, Wayne, NJ) was used for the verification.

In the following, ultrahigh dose rate (UDR) and clinical dose rate (CDR) represent the dose rates that correspond to a beam current of 45 and 1.5 nA at the entrance of the nozzle, respectively. The corresponding dose rates were 325 and 8 Gy/min at the Bragg peak and 114 and 1.75 Gy/min at the plateau for UDR and CDR, respectively. For CDR, the accuracy of the dose measured by the parallel ion chamber was sufficient. For UDR, however, the ion recombination effect cannot be ignored for both the parallel ion chamber and the dose monitor on the beamline, the latter of which was also an ion chamber. In fact, the ion collection efficiency for UDR was 5% lower than that for CDR. Therefore, we performed the dose measurement for UDR in the following way. First, the lateral dose profile at the depth of the cell position was obtained for the CDR in an extensive region including the point P , which was outside of the irradiation field, where the dose was 3% of the dose delivered to the cell containing area. We also measured the dose per monitor unit (DMU) at point P for UDR. As the DMU measurement at P was reliable even for the UDR, the DMU for the UDR in the irradiation field were obtained from the dose profile for CDR and the DMU at point P (see Fig. 4). During the irradiation

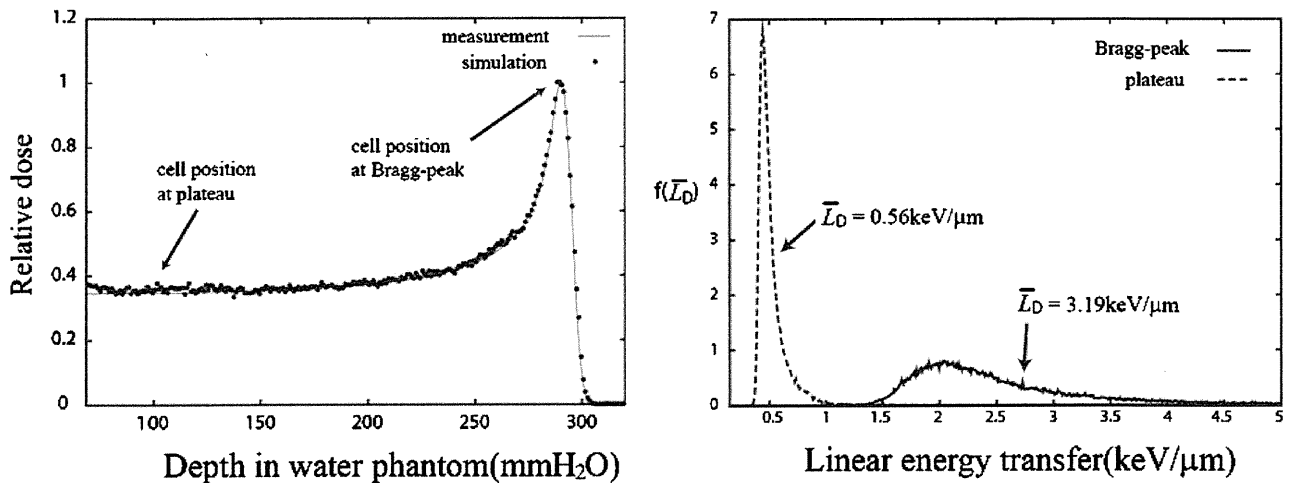


FIG. 3. (Left) Depth-dose profile of the present experiment. The depth-dose measurement was performed in a water phantom. The dots were the results of a GEANT4 simulation. Cell positions are indicated. (Right) The LET distributions at the Bragg peak (solid line) and plateau (dotted line) were calculated by a GEANT4 simulation. In the figure, the distribution has been normalized so that the integral of the distribution $f(L_D)$ is unity.

of the cells, GafChromic EBT film was placed just in front of the each flask and the dose at the moment of irradiation was measured directly. We took advantage of the fact that the optical density (OPD) of the film does not vary with the dose rate, although it does depend on LET.¹⁷ The data points produced by the clinical dose rate were used to determine the OPD dose curve by the weighted least-squares method as follows: $OPD = A + B \times \exp(-C \cdot \text{dose})$, where A, B, and C are the fitting parameters. The fit was good with a reduced χ -square value of 1.7–2.0. All the data points produced at the ultrahigh dose rate were within one sigma deviation from the OPD curve, which indicates that the abovementioned dose calibration method worked well.

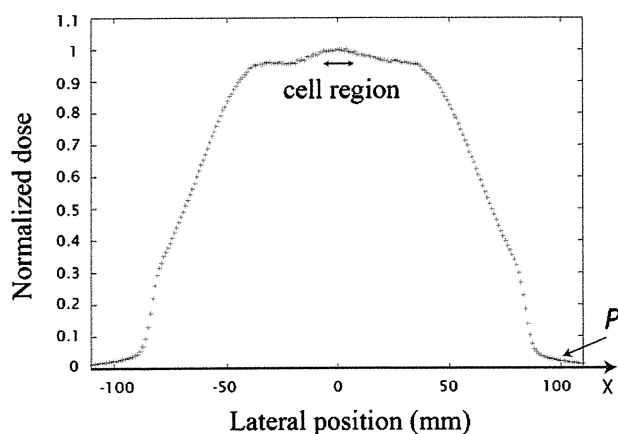


FIG. 4. The lateral dose profile at the cell position depth. The dose was normalized so that the dose at the center of the cell region represented unity. The measurement was performed at the CDR in an extensive region including point $P(x=100)$, which was outside of the irradiation field. The dose at P was 3% of that delivered to the cell containing area. The DMU produced by the UDR at an arbitrary lateral position was determined by the DMU measurement at P for UDR and extrapolation from this profile curve.

In this experiment, in order to obtain a stable proton beam, the timing of the beam initiation was controlled by tuning the radio frequency of the cyclotron. The beam intensity was stabilized to within 4 ms and the variation of the beam current was kept within 2.5% and 15.7% for 45 and 1.5 nA beams, respectively.

II.C. Cell culture and colony formation assay

HSG cells (JCRB1070:HSGc-C5) were used for the experiments. This is a standard reference cell line used for RBE intercomparison of proton facilities in Japan, Korea, etc.^{7,18} Eagle's minimum essential medium (M5655, Sigma, Tokyo, Japan) supplemented with 10% fetal bovine serum and antibiotics (100 U/ml penicillin and 100 $\mu\text{g}/\text{ml}$ streptomycin) was used as the culture medium.

Subcultured cells were harvested and seeded in a slide chamber flask at about $1.5\text{--}2.0 \times 10^5$ cells/flask with 3 ml of the medium and incubated in a 5% CO_2 incubator at 37 °C for 2 days prior to the experiment. The flasks were filled with additional medium 1 day before the experiment and then returned to the incubator.

After being irradiated, the samples were rinsed twice with phosphate buffered saline (PBS), soaked once with 0.025% trypsin, and kept at 37 °C in the remaining trypsin for 4 min before being harvested. The cells were collected in an appropriate volume (2–3 ml) of fresh medium and the cell concentrations were counted by a particle analyzer (Coulter Z1). The cell suspension was diluted using medium, seeded in three 6 cm culture dishes (Falcon 3002) so that there were approximately 100 surviving cells per dish, and incubated in an incubator for 13 days. The colonies in the dishes were rinsed with PBS, fixed with a 10% formalin solution in PBS for 10–15 min, rinsed with tap water, stained with a 1% methylene blue solution, rinsed again with tap water, and

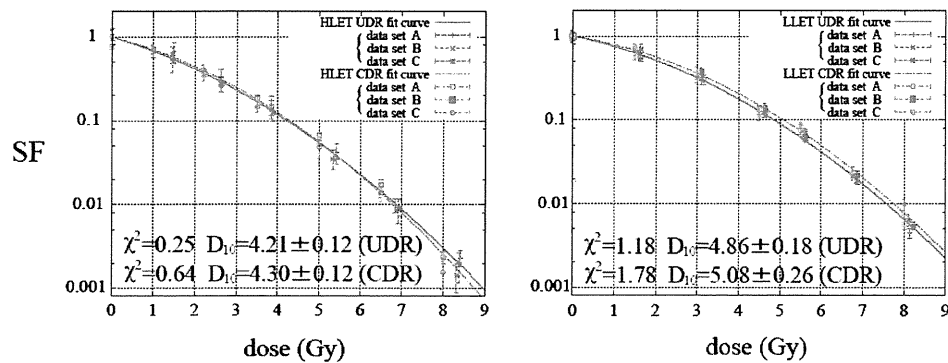


Fig. 5. Survival curves for HSG cells at the Bragg peak (left) and the plateau (right). All data points were fitted by the LQ model. HLET and LLET indicate high and low LET, respectively, and UDR and CDR indicate ultrahigh and clinical dose rate, respectively.

dried in air. Colonies consisting of more than 50 cells were counted under a stereomicroscope as the number of viable cells.

II.D. Analysis of the survival curve and RBE ratios

Doses ranging from 1.0 to 8.0 Gy were delivered at each dose rate and each LET. The irradiation time was 0.2–1.5 s (UDR) and 8–60 s (CDR) at Bragg peak and 0.5–4.2 s (UDR) and 34–274 s (CDR) at plateau, respectively. Three independent cell samples (denoted as A, B, and C) were exposed for each experimental condition. The plating efficiency of unirradiated cells was higher than 80%. In all cases, the surviving fraction is presented as the mean \pm standard deviation (SD) of three replicates. The sensitivity coefficients α and β were calculated by curve-fitting all the data using the weighted least-squares method and the LQ-model equation, $SF = \exp(-\alpha D - \beta D^2)$. Here, SF stands for the surviving fraction and D is the absorbed dose to the cells. For the minimization, the Marquardt–Levenberg algorithm was used. D_{10} values (the dose that reduced cell survival to 10%) were obtained from the α and β parameters for each survival data set. From the D_{10} values, we derived the ratios of RBE for different dose rates and LET

$$RRBE(a/b) = \frac{RBE(a)}{RBE(b)}, \quad (1)$$

where a and b indicate UDR and CDR, or high and low LET, respectively. Since we are interested in the variation of RBE over the dose rate, we do not need to use a particular radiation quality as a reference for RBE. The SDs of D_{10} and RRBE value were calculated by the Gaussian error propagation from σ_α and σ_β (SD of α and β , respectively). In addition, differences of estimated SF at $D=2, 4, 6,$ and 8 Gy, which were obtained from the abovementioned curve fitting to the independent data sets (A, B, and C), according to the dose rates and LET were tested with unpaired t-test. The error in absorbed dose was assumed to be negligible.

III. RESULTS

The measured data and fitting curves are illustrated in Fig. 5. The left and right figures show SF at the Bragg peak and

plateau, respectively. The reduced χ -square values and the D_{10} values are included in the figure.

At the Bragg peak, the fitted parameters were $\alpha=0.348 \pm 0.018$ (Gy^{-1}) and $\beta=0.047 \pm 0.003$ (Gy^{-2}) for UDR and $\alpha=0.294 \pm 0.019$ (Gy^{-1}) and $\beta=0.056 \pm 0.003$ (Gy^{-2}) for CDR. The D_{10} values were 4.21 ± 0.12 and 4.30 ± 0.12 , respectively, and the ratio of RBE was $RRBE(\text{CDR}/\text{UDR})=0.98 \pm 0.04$.

At the plateau, the fitted parameters were $\alpha=0.237 \pm 0.022$ (Gy^{-1}) and $\beta=0.049 \pm 0.003$ (Gy^{-2}) for UDR and $\alpha=0.183 \pm 0.029$ (Gy^{-1}) and $\beta=0.053 \pm 0.005$ (Gy^{-2}) for CDR. The D_{10} values were 4.86 ± 0.18 and 5.08 ± 0.26 , respectively, and the RBE ratio was $RRBE(\text{CDR}/\text{UDR})=0.96 \pm 0.06$, which shows that the dose rate independence of RBE found at the Bragg peak also holds at the plateau.

On the other hand, there are more than 15% differences in RBE between high and low LET for each dose rate: $RRBE(\text{Bragg peak}/\text{plateau})=1.15 \pm 0.05$ (UDR) and 1.18 ± 0.07 (CDR), indicating that RBE enhancement at the Bragg peak cannot be ignored for both UDR and CDR.

P-values in unpaired t-tests for the difference of SFs according to the dose rates and LET were shown in Table 1. There were no statistically significant differences of SFs between CDR and UDR at all above points in Bragg peak and plateau, while significant differences of SFs between Bragg peak and plateau was observed ($p < 0.05$).

IV. DISCUSSION

This study revealed that RBE does not depend on the dose rate between 1.75 and 325 Gy/min at the Bragg peak or plateau when it was estimated with SF of HSG cell line. Recently, experiments involving much higher dose rates produced by the Munich tandem accelerator have been performed by Schmid *et al.*^{8,9} They irradiated HeLa cells with 3 Gy of laser accelerated 20 MeV protons (equivalent to a dose-averaged LET of 2.66 keV/ μm) and obtained RBE of 1.06 ± 0.10 and 1.05 ± 0.11 for two experiments with irradiation times of 100 and 23 ms (the corresponding mean dose rates were estimated to be 1.8 and 7.8 kGy/min), respectively. Although their RBE was not defined in precisely the

TABLE I. Estimated SFs and the P-values in unpaired t-test for the difference of SFs according to the dose rate and LET.

Dose (Gy)	Surviving fraction (standard deviation)				P-values for the difference of surviving fractions			
	Bragg peak		Plateau		UDR vs CDR		Bragg peak vs plateau	
	UDR	CDR	UDR	CDR	Bragg peak	Plateau	UDR	CDR
2	0.423 (0.024)	0.439 (0.016)	0.540 (0.048)	0.550 (0.017)	0.41	0.75	0.02	<0.01
4	0.120 (0.010)	0.122 (0.009)	0.192 (0.025)	0.200 (0.011)	0.76	0.64	0.01	<0.01
6	0.023 (0.003)	0.022 (0.002)	0.045 (0.005)	0.048 (0.005)	0.68	0.47	<0.01	<0.01
8	0.003 (0.001)	0.002 (0.000)	0.007 (0.000)	0.008 (0.001)	0.33	0.38	<0.01	<0.01

same way as ours, our results offered additional data to support that the RBE would not change within the range from the clinical dose rate to ultrahigh dose rate of 7.8 kGy/min. Therefore we submit that the same RBE in CDR is available for one-shot radiation therapy. The reason for the dose rate independence may be that in both our experiment and theirs, the irradiation time scale is much smaller than the repair half time.^{19,20} Although we used a mono energy proton beam in this experiment, dose rate independence of the survival curve between high and low LET is also applicable in PRT using SOBP, because LET in the SOBP method distributes the same range as that used in this study.

On the contrary, SFs of HSG cells are substantially dependent on LET. In fact, our data suggested that more than 15% of RBE difference exists between Bragg peak ($\bar{L}_D=3.19$ keV/ μ m) and plateau ($\bar{L}_D=0.56$ keV/ μ m). In Bettega *et al.*,^{21,22} it was shown that proton RBE determined via the formation of micronuclei in a heteroploid cell line with an epithelioid morphology (EUE line with a modal number of 60 chromosomes) were 1.7, 1.3, and 1.0 for proton beams of 8, 12, and 31 MeV, which had LET of 5.5, 4.0, and 1.8 keV/ μ m, respectively.¹⁶ Our results, as well as the previous measurement of RBE at SOBP center,⁷ were consistent with their results. This study provides additional evidence supporting that there is significant difference of RBE between the Bragg peak and plateau. Since critical organs such as brain stem, cord, and optical nerves are frequently located at the close proximity of the distal fall-off of Bragg peak, the extensive measurement of RBE beyond Bragg peak is urgently required and it should be included in the dose calculation in proton beam treatment planning.²³

This study may also indicate that we can use the present RBE for scanning proton therapy as long as the dose rate is within the range of that was used in this experiment. In the scanning irradiation, the temporal structure of the dose rate becomes important especially when a rescanning technique is used to attain dose spatial uniformity,²⁴ but our result showed the temporal variation of the dose rate does not affect the RBE.

A weakness of this study is the fact that in practice, the tissues in the plateau region are different from those in the Bragg peak region, so investigations on one cell line may not tell the whole story. We will investigate this point further in the near future.

V. CONCLUSIONS

We conclude that there were no significant differences in the survival curves of HSG cells produced by proton dose rates of 8 and 325 Gy/min at the Bragg peak ($\bar{L}_D=3.19$ keV/ μ m) and 1.75 and 114 Gy/min at the plateau ($\bar{L}_D=0.56$ keV/ μ m) ($p>0.05$). The RBE ratios were $RRBE(CDR/UDR)=0.98 \pm 0.04$ at the Bragg peak and 0.96 ± 0.06 at the plateau. Therefore, the present RBE can be used in therapeutic planning for one-shot radiation therapy. Conversely, significant RBE deviation between high and low LET was found at both the UDR and CDR: $RRBE(\text{Bragg peak}/\text{plateau})=1.15 \pm 0.05(\text{UDR})$ and $1.18 \pm 0.07(\text{CDR})$. Therefore, RBE enhancement at the Bragg peak and distal fall-off should be carefully considered.

ACKNOWLEDGMENTS

The authors would like to thank Kazutomo Matsumura, Ryuichi Ohta, Hiroyuki Suzuki, Tomohiro Toda, Takeya Taniyama, Takuya Shimoju, Atsushi Sakamoto, and Kenji Yamazaki for their most professional support. T.M. received a grant from the Foundation for the Promotion of Cancer Research.

^{a)} Author to whom correspondence should be addressed. Electronic addresses: tmk314@gmail.com and matsuura@med.hokudai.ac.jp; Telephone: +81-11-706-5974; Fax: +81-11-706-7876.

¹K. Nihei, T. Ogino, S. Ishikura, and H. Nishimura, "High-dose proton beam therapy for stage I non-small-cell lung cancer," *Int. J. Radiat. Oncol. Biol. Phys.* **65**, 107–111 (2006).

²M. Kawashima, J. Furuse, T. Nishio, M. Konishi, H. Ishii, T. Kinoshita, M. Nagase, K. Nihei, and T. Ogino, "Phase II study of radiotherapy employing proton beam for hepatocellular carcinoma," *J. Clin. Oncol.* **23**, 1839–1846 (2005).

³H. Tsujii, T. Kamada, M. Baba, H. Tsuji, H. Kato, S. Kato, S. Yamada, S. Yasuda, T. Yanagi, H. Kato, R. Hara, N. Yamamoto, and J. Mizoe, "Clinical advantages of carbon-ion radiotherapy," *New J. Phys.* **10**, 075009–075024 (2008).

⁴T. Miyamoto, M. Baba, M. Nakajima, T. Yashiro, K. Kagei, N. Hirasawa, T. Sugawara, N. Yamamoto, M. Koto, H. Ezawa, K. Kadono, H. Tsujii, J. Mizoe, K. Yoshikawa, S. Kandatsu, and T. Fujisawa, "Carbon ion radiotherapy for stage I non-small cell lung cancer using a regimen of four fractions during 1 week," *J. Thorac. Oncol.* **2**(10), 916–926 (2007).

⁵E. Pedroni *et al.*, "The PSI Gantry 2: A second generation proton scanning gantry," *Med. Phys.* **14**, 25–34 (2004).

⁶K. Ando, Y. Furusawa, M. Suzuki, K. Nojima, H. Majima, S. Koike, M. Aoki, W. Shimizu, Y. Futami, T. Ogino, S. Murayama, and H. Ikeda, "Relative biological effectiveness of the 235 MeV proton beams at the National Cancer Center Hospital East," *J. Radiat. Res. (Tokyo)* **42**, 79–89

- (2001).
- ⁷Y. Furusawa, M. Aoki, Y. Shino, R. Lee, G. Zhou, N. Takai, M. Monobe, T. Fukawa, Y. Miyato, and G. Kagiya, "Intercomparison of radiobiological RBE among Japanese proton therapy facilities," in Proceedings of the World Congress on Medical Physics and Biomedical Engineering, Sydney, Australia, August 2003.
- ⁸T. E. Schmid, G. Dollinger, A. Hauptner, V. Hable, C. Greubel, S. Auer, A. A. Friedl, M. Molls, and B. Röper, "No evidence for a different RBE between pulsed and continuous 20 MeV protons," *Radiat. Res.* **172**, 567–574 (2009).
- ⁹T. E. Schmid, G. Dollinger, V. Hable, C. Greubel, O. Zlobinskaya, D. Michalski, M. Molls, and B. Röper, "Relative biological effectiveness of pulsed and continuous 20 MeV protons for micronucleus induction in 3D human reconstructed skin tissue," *Radiother. Oncol.* **95**, 66–72 (2010).
- ¹⁰K. Shinohara, H. Nakano, N. Miyazaki, M. Tsgo, and R. Kodama, "Effects of single-pulse (≤ 1 ps) x-rays from laser-produced plasmas on mammalian cells," *J. Radiat. Res. (Tokyo)* **45**(4), 509–514 (2004).
- ¹¹H. B. Michaels, E. R. Epp, C. C. Ling, and E. C. Peterson, "Oxygen sensitization of CHO cells at ultrahigh dose rates: Prelude to oxygen diffusion studies," *Radiat. Res.* **76**, 510–521 (1978).
- ¹²C. C. Ling, L. E. Gerweck, M. Zaidler, and E. Yorke, "Dose-rate effects in external beam radiotherapy redux," *Radiother. Oncol.* **95**(3), 261–268 (2010).
- ¹³T. Nishio, "Present status and planning of facilities for proton and heavy ion cancer treatment in Japan. III. Present state of proton beam treatment facility in the National Cancer Center Hospital East," *J. At. Energy Soc.* **41**, 1134–1138 (1999).
- ¹⁴T. Tachikawa, T. Sato, T. Ogino, and T. Nishio, "Proton beam therapy facilities of the National Cancer Center East Hospital," *Radiat. Indust.* **84**, 48–53 (1999).
- ¹⁵T. Aso, A. Kimura, S. Tanaka, H. Yoshida, N. Kanematsu, T. Sasaki, and T. Akagi, "Verification of the dose distributions with Geant4 simulation for proton therapy," *IEEE Trans. Nucl. Sci.* **52**, 896–901 (2005).
- ¹⁶J. F. Janni, "Calculations of energy loss, range, path length, straggling, multiple scattering, and the probability of inelastic nuclear collisions for 0.1- to 1000-MeV protons," AFWL Technical Report No. 65-150 (Kirtland AFB, 1966).
- ¹⁷D. Kirby, S. Green, H. Palmans, R. Hugtenburg, C. Wojnecki, and D. Parker, "LET dependence of GafChromic films and an ion chamber in low-energy proton dosimetry," *Phys. Med. Biol.* **55**, 417–433 (2010).
- ¹⁸H. J. Baek, T. H. Kim, D. Shin, J. W. Kwak, D. W. Choo, S. B. Lee, Y. Furusawa, K. Ando, S. S. Kim, and K. H. Cho, "Radiobiological characterization of proton beam at the National Cancer Center in Korea," *J. Radiat. Res. (Tokyo)* **49**(5), 509–515 (2008).
- ¹⁹Y. Shibamoto, M. Ito, C. Sugie, H. Ogino, and M. Hara, "Recovery from sublethal damage during intermittent exposures in cultured tumor cells: Implications for dose modification in radiosurgery and IMRT," *Int. J. Radiat. Oncol. Biol. Phys.* **59**, 1484–1490 (2004).
- ²⁰H. Ogino, Y. Shibamoto, C. Sugie, and M. Ito, "Biological effects of intermittent radiation in cultured tumor cells: Influence of fraction number and dose per fraction," *J. Radiat. Res. (Tokyo)* **46**, 401–406 (2005).
- ²¹D. Bettega, M. Bombana, T. Pelucchi, A. Poli, L. Tallone Lombardi, and A. M. Fuhrman Conti, "Multinucleate cells and micronucleus formation in cultured human cells exposed to 12MeV protons and c-rays," *Int. J. Radiat. Biol.* **37**, 1–9 (1980).
- ²²D. Bettega, S. Dubini, A. M. Fuhrman Conti, T. Pelucchi, and L. Tallone Lombardi, "Chromosome aberrations induced by protons up to 31 MeV in cultured human cells," *Radiat. Environ. Biophys.* **19**, 91–100 (1981).
- ²³J. J. Wilkens and U. Oelfke, "A phenomenological model for the relative biological effectiveness in therapeutic proton beams," *Phys. Med. Biol.* **49**, 2811–2825 (2004).
- ²⁴J. Gueulette, H. Blattmann, E. Pedroni, A. Coray, B. M. De Coster, P. Mahy, A. Wambersie, and G. Goitein, "Relative biologic effectiveness determination in mouse intestine for scanning proton beam at Paul Scherrer Institute, Switzerland. Influence of motion," *Int. J. Radiat. Oncol. Biol. Phys.* **62**(3), 838–845 (2005).

Measurement and verification of positron emitter nuclei generated at each treatment site by target nuclear fragment reactions in proton therapy

Aya Miyatake^{a1}

Department of Nuclear Engineering and Management, Graduate School of Engineering,
University of Tokyo, 2-11-16 Yayoi, Bunkyo-ku, Tokyo 113-0032, Japan

Teiji Nishio

Particle Therapy Division, Research Center for Innovative Oncology, National Cancer Center, Kashiwa,
6-5-1 Kashiwano-ha, Kashiwa-shi, Chiba 277-8577, Japan and Department of Radiology, Graduate
School of Medicine, University of Tokyo, 7-3-1 Hongo, Bunkyo-ku, Tokyo 113-8655, Japan

Takashi Ogino

Particle Therapy Division, Research Center for Innovative Oncology, National Cancer Center, Kashiwa,
6-5-1 Kashiwano-ha, Kashiwa-shi, Chiba 277-8577, Japan

Nagahiro Saijo and Hiroyasu Esumi

National Cancer Center, Kashiwa, 6-5-1 Kashiwano-ha, Kashiwa-shi, Chiba 277-8577, Japan

Mitsuru Uesaka

Nuclear Professional School, School of Engineering, University of Tokyo, 22-2 Shirane-shirakata, Tokai,
Naka, Ibaraki 319-1188, Japan

(Received 6 July 2009; revised 21 June 2010; accepted for publication 21 June 2010;
published 29 July 2010)

Purpose: The purpose of this study is to verify the characteristics of the positron emitter nuclei generated at each treatment site by proton irradiation.

Methods: Proton therapy using a beam on-line PET system mounted on a rotating gantry port (BOLPs-RGp), which the authors developed, is provided at the National Cancer Center Kashiwa, Japan. BOLPs-RGp is a monitoring system that can confirm the activity distribution of the proton irradiated volume by detection of a pair of annihilation gamma rays coincidentally from positron emitter nuclei generated by the target nuclear fragment reactions between irradiated proton nuclei and nuclei in the human body. Activity is measured from a start of proton irradiation to a period of 200 s after the end of the irradiation. The characteristics of the positron emitter nuclei generated in a patient's body were verified by the measurement of the activity distribution at each treatment site using BOLPs-RGp.

Results: The decay curves for measured activity were able to be approximated using two or three half-life values regardless of the treatment site. The activity of half-life value of about 2 min was important for a confirmation of the proton irradiated volume.

Conclusions: In each proton treatment site, verification of the characteristics of the generated positron emitter nuclei was performed by using BOLPs-RGp. For the monitoring of the proton irradiated volume, the detection of ^{15}O generated in a human body was important. © 2010 American Association of Physicists in Medicine. [DOI: 10.1118/1.3462559]

Key words: beam on-line PET system, target nuclear fragment reaction, monitoring of proton irradiation, *in vivo* dosimetry

I. INTRODUCTION

Recently, due to rapid technological innovation, it has become possible to provide patients with radiotherapy that can concentrate a high dose onto a tumor. In addition to usual radiotherapy using a photon or electron beam, particle therapy using a large accelerator and an irradiation device is becoming more widely used and various kinds of radiation are used for radiotherapy. When a particle beam is irradiated to a patient's body, it shows a form of depth dose distribution called a Bragg peak in the incidence direction. Particle therapy is able to concentrate a dose onto a tumor using a Bragg peak and also delivers a superior dose distribution for the dose concentration, as well as showing higher biological

effectiveness for the amount of radiation delivered compared to photon and electron beam therapy. So it is considered that particle therapy is very effective even for tumors that are difficult to treat with radiation.

At present, the number of particle therapy facilities has been increasing. Particle therapy means proton therapy or carbon therapy. There are 27 facilities (proton: 24, carbon: Two, both: One) that provide particle therapy including research facilities. Of these, 11 facilities began offering treatment after 2000 (proton: Ten, carbon: 0, both: One).¹ Recently, the increase in the number of facilities and the development of the technology has been remarkable. As for the rate of spread of these facilities, the spread of proton therapy has been more rapid than that of carbon therapy.

In proton therapy with a high dose concentration, if the beam misses its target, it may reduce the curative ratio and damage the organ at risk. Therefore, it is very important to confirm the irradiated volume in a patient undergoing proton therapy.

In one method, target nuclear fragment reactions are used to monitor the proton irradiated volume. This uses the positron emitter nuclei generated in a patient's body from target nuclear fragment reactions between the incident proton nuclei and the nuclei in the patient's body. The irradiated volume is monitored by concurrent detection of a pair of annihilation gamma rays from positron emitter nuclei. In the energy range used for proton therapy (0–250 MeV), C, N, O, and Ca nuclei present in the patient's body react with the incident proton nuclei. Considering the cross section of the reaction, the positron emitter nuclei generated from the target nuclei are ^{10}C , ^{11}C , ^{13}N , ^{15}O , ^{38}K , etc.

Recently, research into the monitoring of the proton irradiated volume based on this principle has become more common^{2–15} and the systems developed can be divided into two types. The first is the beam off-line PET type, which uses commercial PET or PET-CT apparatus installed in a separate room. The other type is a beam on-line PET type, developed using original PET apparatus installed in an irradiation room.

There are some reports of the measurement and simulation of clinical proton therapy using the beam off-line PET type. As for beam on-line PET type, it was reported in non-clinical environments.³ However, only one report has involved measurements at various treatment sites with a beam on-line PET type apparatus and that used the beam on-line PET system mounted on a rotating gantry port (BOLPs-RGp), developed at the National Cancer Center, Kashiwa.¹⁵ The main element of human tissue except adipose tissue and bone is ^{16}O . ^{16}O mainly generates ^{15}O during target nuclear fragment reactions. Therefore, ^{15}O is the kind of positron emitter nuclei generated most abundantly in the human body during proton therapy. As the half-life value of ^{15}O is about 2 min, it is difficult to measure using an off-line type apparatus. Using information about ^{15}O enables the observation of the proton irradiated volume with high precision in a short time. One advantage of the BOLPs-RGp system is that much information concerning ^{15}O is acquired during the monitoring and confirmation of the irradiated volume.

In this study, decay curve data, which were measured as activity using the BOLPs-RGp in every patient and treatment site during proton therapy, were analyzed, and the character-

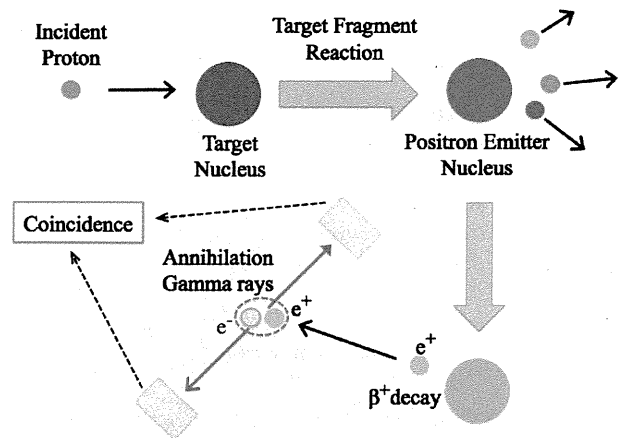


FIG. 1. A diagram demonstrating the monitoring of the proton irradiated volume using target nuclear fragment reactions.

istics of the positron emitter nuclei generated were verified in a patient from which includes sufficient information about ^{15}O was obtained during proton irradiation. This is the first study that has analyzed such data.

In this paper, the BOLPs-RGp apparatus and measurement of activity are described in Sec. II. Measurement and analysis and results and discussion are presented in Sec. III. Section IV discusses the conclusions of this study.

II. MATERIALS AND METHODS

II.A. Target nuclear fragment reactions and imaging of activity in a patient's body

In the energy range of proton therapy, target nuclear fragment reactions [ex. $^{16}\text{O}(\text{p,pn})^{15}\text{O}$, $^{12}\text{C}(\text{p,pn})^{11}\text{C}$,...] occur between the incident proton nuclei and the atomic nuclei in a patient's body. Using the positron emitter nuclei generated from this reaction, it is possible to monitor the proton irradiated volume in a patient's body by detecting its position and intensity with PET apparatus. Figure 1 shows the target nuclear fragment reactions caused by proton irradiation and the method used to identify the positron emitter nuclei generated by this reaction.

The human body is mainly composed of five elements: H, C, N, O, and Ca. Four of these elements, C, N, O, and Ca, cause target nuclear fragment reactions in the energy range

TABLE I. Human body tissue composition (%).

	H	C	N	O	Ca	Others
Average soft tissue	10.6	28.6	2.6	57.5	—	0.7
Adipose tissue	11.4	59.9	0.7	27.7	—	0.3
Liver	10.2	13.9	3.0	71.6	—	1.3
Lung	10.3	10.5	3.1	74.9	—	1.2
Prostate	10.5	25.6	2.7	60.2	—	1.0
Skeleton-cranium	5.0	21.2	4.0	43.5	17.6	8.7

TABLE II. Target nuclear fragment reaction channel and essential positron emitter nuclei for imaging using BOLPs-RGp against main elemental composition of ^{12}C , ^{14}N , ^{16}O , and ^{40}Ca in human body.

Target nuclei	Generated positron emitter nuclei	Half-life value
^{12}C	^{10}C	19.2 s
	^{11}C	20.4 min
^{14}N	^{10}C	19.2 s
	^{11}C	20.4 min
	^{13}N	9.97 min
	^{14}O	70.8 s
^{16}O	^{15}O	122 s
	^{10}C	19.2 s
	^{11}C	20.4 min
	^{13}N	9.97 min
	^{14}O	70.8 s
^{40}Ca	^{15}O	122 s
	^{38}K	7.63 min
	^{38}Ca	0.447 s
	^{39}Ca	0.860 s

of proton therapy. The composition of the human body tissues at common proton therapy treatment sites is shown in Table I.¹⁶

Table II shows the typical reaction channels of target nuclear fragment reactions between the incident proton nuclei and target nuclei in the human body that generate positron emitter nuclei, which were obtained by monitoring the irradiated volume and the half-life value of the positron emitter nuclei generated by the reactions.¹⁷ The positron emitter nuclei of second-order and minute-order half-life value with mb-order target nuclear fragment reaction cross section generated in main elemental composition of ^{12}C , ^{14}N , ^{16}O , and ^{40}Ca of human body are important for the activity imaging. Therefore, ^9C of 127 ms half-life time and ^{13}O of 9 ms half-life time are not used for the activity imaging. Figure 2 shows the experimental values of the cross section of the target nuclear fragment reactions.¹⁷

II.B. Beam on-line PET system mounted on a rotating gantry port: BOLPs-RGp

The BOLPs-RGp installed on the proton beam line in our treatment room in the National Cancer Center, Kashiwa, was developed for monitoring the proton irradiated volume. The apparatus uses opposing detector heads of planar type with a high position resolution (Fig. 3).¹⁵ Each detector consists of BGO crystals with a crystal size of $2 \times 2 \times 20 \text{ mm}^3$. The field of view (FOV) at the isocenter is $164.8 \times 167.0 \text{ mm}^2$. The detector heads opposite each other installed along the axis of the proton beam direction rotate together with the rotating gantry system, and the distance between the opposing detector heads can be adjusted from 30 to 100 cm. The maximum collection rate of the data for the coincident detection of this system is about 1 mega count per second. Detection efficiency of each distance of detector heads of 30 to 100 cm was calibrated using the thin-flat acrylic container filled with ^{18}F solution. 3-D imaging of activity is recon-

structed from the detection data of the planar detector by using maximum likelihood algorithm, taking into consideration the attenuation coefficient of 511 keV gamma rays in the patient's body calculated by the patient's CT image data. In the experiment using a ^{22}Na point source, position resolution of measured activity with the distance between detector heads of 50 cm was about 2 mm of the full width at half maximum at isocenter in the FOV. The change of the position resolution depending on the increase of the distance between detector heads is about 1 mm.¹⁸ The deterioration of the position resolution when moving the point source in the planar plane is smaller than 1 mm in the FOV.¹⁸ In the measurement of the positron emitter nuclei generated in a patient's body by the proton irradiation, the dead time and random coincidence correction of detection are a negligible value for weak intensity of the activity. The measured data is stored using a formatted data with a list mode. The on-off time points of beam irradiation and synchronization with the organ motion caused by respiration are recorded in the data and the image can be restructured according to this information. The time jitter between end of irradiation and timestamp of activity data is under 20 ms. The activity data in the irradiation field of each patient are managed throughout each treatment day.

The data detected by BOLPs-RGp is verified using the Viewer of Activity for Clinical Analysis (VACA) (SGI, Japan), developed for display and analysis tool of the activity. The images of measured activity and calculated dose are viewed on the CT image for a proton treatment planning. Differences in the daily measured activity of each patient's irradiation port can be analyzed using the data collected by VACA. The BOLPs-RGp enables the measurement of the position and intensity of positron emitter nuclei in a human body by detecting the pairs of annihilation gamma rays (511 keV) emitted from positron emitter nuclei generated in a patient's body by proton irradiation.

II.C. The measurement of activity using BOLPs-RGp

Proton therapy is provided using the BOLPs-RGp in the National Cancer Center, Kashiwa.¹⁵ Activity is measured from a start of proton irradiation to a period of 200 s after the end of the irradiation. The only activity data measured during the 200 s after the end of the irradiation are used to construct the activity distribution image because the data that are measured during proton irradiation includes x rays, gamma rays, and the neutron beam. The quality of the activity image becomes markedly worse in their presence of background. Furthermore, high radiation decreases the accuracy of the detector. In this coincident radiation detection system in irradiation of clinical dose, the residual neutron immediately after the end of beam irradiation is equal to the background level of natural radiation. Therefore, the influence for activity imaging is disregarded. The time of 200 s after proton beam irradiation was chosen according to the intensity of activity estimated from the results of the statistical error of detection events and limitation of time for smoothly clinical use. The decay characteristics of the activity count, which are mea-

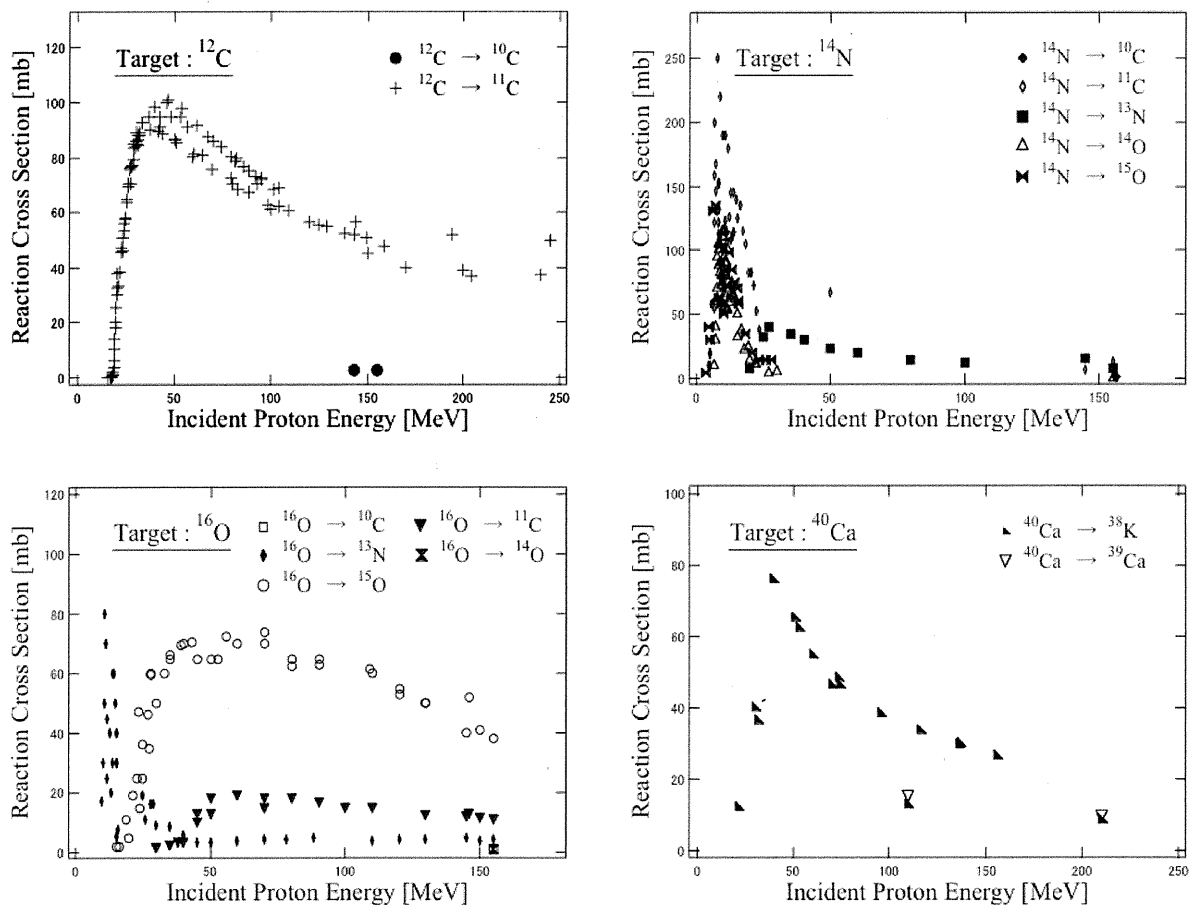


FIG. 2. The experimental values of the nuclear reaction cross section compared to the incident proton energy.

sured every second during the measurement period, were verified for common treatment sites such as the head and neck, liver, lung, and prostate. Five cases were chosen for each treatment site, one port was performed from the irradiation ports planned in each case, and three data sets were

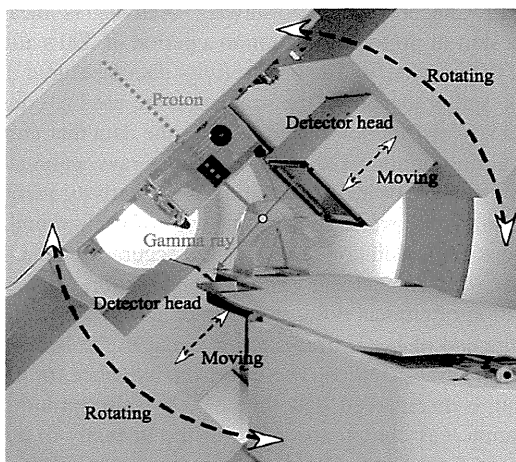


FIG. 3. Setup of the BOLPs-RGp, which is mounted on the rotating gantry port of our proton treatment room.

selected from the series of treatments for data analysis. In the case of lung tumor, the fractional dose was irradiated with proton beam of two directions. The verified irradiation conditions and the distance of detection are shown in Table III. The irradiation of the liver and lung was synchronized with the organ motion caused by respiration. The way of the gated lung and liver irradiation in our hospital is beam irradiation performed at expirations with the sensor of a pressure putting on patient's abdomen. The typical intervals in the case gated liver and lung tumor irradiation are 2 s for proton irradiation and 2 s for no proton irradiation.

III. RESULTS AND DISCUSSION

III.A. Measured activity distributions

The activity distributions shown in Fig. 4 were examples in each treatment site selected from about 2000 clinical images obtained from the measured data with the BOLPs-RGp. In Fig. 4(a), the prescribed fractional dose was 2.5 GyE [= [Gy] × RBE (= 1.1 = constant)], the gantry angle was 10°, the distance between opposing detector heads was 70 cm, and irradiation was delivered to the head and neck. The parameters for the other organs were as follows: 3.8 GyE, 270°, and 60 cm in the liver; 4.0 GyE, 310°, and 80 cm

TABLE III. The irradiation conditions of the verified patients.

Site	Clinical treatment planning			Beam information for data analysis				BOLPs-RGp	
	Patient ID	Fractional dose (GyE)	Total dose (GyE)	Irradiated dose (GyE)	E (MeV)	Maximum beam range (mmWEL) ^a	SOBP (mm)	Field size (mm ϕ)	Distance of between detector heads (cm)
Head and neck	a	2.5	65	2.5	130.2	122.9	90	103.0	40
	b	2.5	65	2.5	111.5	93.9	80	99.6	40
	c	2.5	65	2.5	116.7	101.6	70	111.1	40
	d	2.0	70	2.0	131.3	124.6	80	202.7	60
	e	2.5	65	2.5	97.9	75.0	60	86.4	50
Liver	a	3.8	76	3.8	103.8	82.9	50	74.7	60
	b	3.8	76	3.8	132.5	126.6	60	95.3	70
	c	2.5	65	2.5	133.1	127.6	80	174.3	50
	d	3.8	76	3.8	122.0	109.7	70	60.8	80
	e	2.5	65	2.5	132.9	127.3	60	107.7	60
Lung	a	4.0	80	2.0	127.9	119.2	60	84.4	60
	b	4.0	80	2.0	125.0	114.5	60	105.3	60
	c	4.0	80	2.0	69.6	41.4	30	60.6	50
	d	4.0	80	2.0	102.0	80.5	30	56.6	60
	e	4.0	80	2.0	98.3	75.4	50	70.1	80
Prostate	a	2.0	74	2.0	186.7	229.7	50	80.0	50
	b	2.0	74	2.0	180.3	216.1	50	181.6	50
	c	2.0	74	2.0	184.1	224.1	60	88.3	50
	d	2.0	74	2.0	182.1	219.9	60	187.4	50
	e	2.0	74	2.0	192.5	242.0	60	86.4	50

^aWEL: Water equivalent length.

in the lung; and 2.0 GyE, 270°, and 50 cm in the prostate. The activity distribution observed outside the target volume is for the scattering effect of annihilation gamma rays in a patient's body. The obtained activity images using BOLPs-RGp showed the proton irradiated volume in patient's bod-

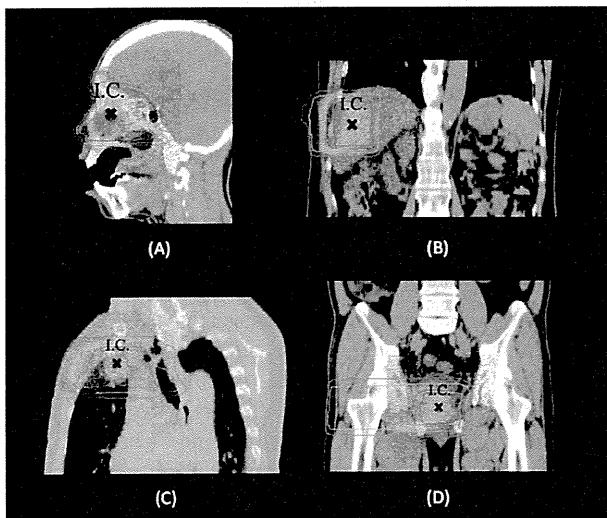


FIG. 4. Dose distribution calculated with the proton treatment planning system and activity distribution measured with the BOLPs-RGp on CT image in (a) head and neck, (b) liver, (c) lung, and (d) prostate. The isodose line of 100% is red, 80% yellow green, 50% light blue, and 20% purple. The activity distribution is relative distribution, which is represented by red for high value and blue for low.

ies. The mean detection rate over the 200 s measurement period at each treatment site was 0.5 kcps in the head and neck, 0.7 kcps in the liver, 0.2 kcps in the lung, and 1.5 kcps in the prostate. The activity count in the bone was high. As the density of bone is high, it is thought that a high amount of activity is generated by target nuclear fragment reactions. The measured activity distributions almost correspond to the calculated dose distributions on CT images for proton treatment planning anatomically except a field of a proton beam range. Target nuclear fragment reactions are occurred by the kinetic energy of incident proton above binding energy of the nuclei. Due to this, positron emitter nuclei are not generated just before the beam stops. Also, no activity distribution is observed before the depth point of the proton beam range and the Bragg peak.

From previous patient study of the beam off-line PET type, the activity measured after proton irradiation in proton irradiated volume of both bone and the subcutaneous adipose tissue was higher than the surroundings.¹³⁻¹⁵ However, in this study of beam on-line PET type, high activity was observed in area of bone while the activity in the subcutaneous adipose tissue was low. This phenomenon was caused by the difference of tissue's component which leads to the difference of positron emitter nuclei generated in the tissue. There are many ¹²C nuclei in adipose tissue in comparison with other tissues shown in Table I. Therefore, many ¹¹C nuclei of long half-life were generated in adipose tissue. On the other hand, ^{38,39}Ca and ^{14,15}O positron emitter nuclei of short half-life were generated in skeleton-cranium (see Table I). The

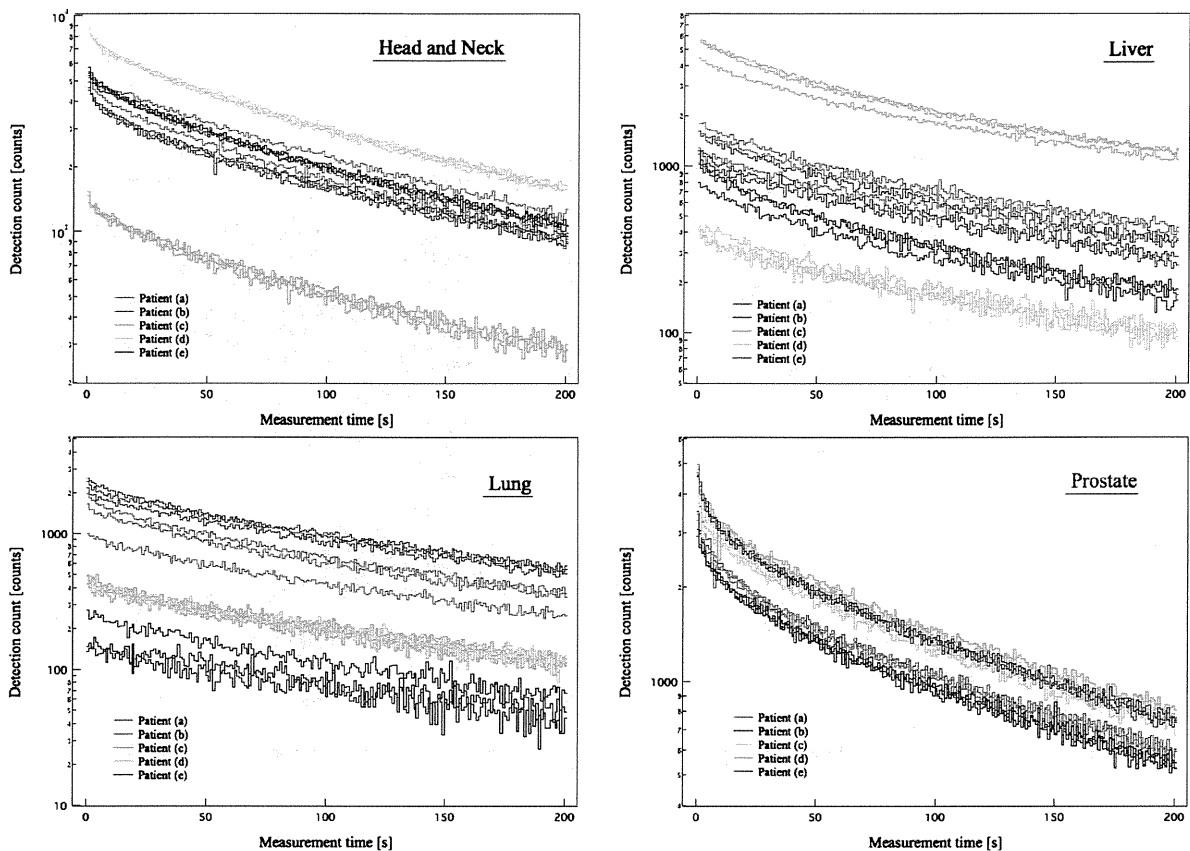


FIG. 5. Decay curves measured during the 200 s after irradiation at each treatment site.

activity distribution obtained after proton irradiation is different by half-life value of various kinds of positron emitter nuclei depending on the time from the stop of irradiation to the start of activity measurement by PET or PET-CT apparatus.

The washout effect of the activity of positron emitter nuclei generated by proton irradiation in human body should be considered for the analysis. Previous animal studies reported that the coefficient of the biological washout effect was estimated to be the around 60% of the total activity.^{19,20} These studies used ^{10}C , ^{11}C , and ^{12}C beams. And the result was about the biological washout effect of ^{10}C and ^{11}C implanted ions or ^{11}C resulting from autoactivation of ^{12}C beams. Fiedler *et al.*²¹ (2008) studied the quantitative verification of the activity of positron emitter nuclei generated by target nuclear fragment reactions and described significance of washout effect in patient studies using ^{12}C beam. And there are some reports that research washout effect of ^{15}O activity generated by photonuclear reaction using high-energy x-ray irradiation.^{22,23} Our previous study mentioned the washout effect of liver of patient in proton therapy.¹⁵ One of the deterioration of images obtained from the measured activity using BOLPs-RGp will be for the washout effect. However, a detail of a physical process of physiological washout is still

unsolved under investigation around the world. Therefore, it is difficult to estimate the quantitative contamination of a washout effect in the measured activity.

III.B. Decay curve of measured activity

The decay curves measured at each site are shown in Fig. 5. The value of the vertical axis is different for every patient and treatment. This is due to differences in the composition of the patients' bodies, the prescribed fractional dose, the distance between the detector heads, and the proton beam irradiation time. As for the liver and lung, there were differences in the irradiation time of each patient and the proton beam was irradiated by synchronization with respiration.

Half-life values of generated positron emitter nuclei shown in Table II are divided with about 1 s of ^{38}Ca and ^{39}Ca , 20 s of ^{10}C , 1–2 min of ^{14}O , ^{15}O , and 7–20 min of ^{11}C , ^{13}N , and ^{38}K . The activity of generated positron emitter nuclei in a patient's body is measured during 200 s after proton irradiation. In the activity measurement time, the activity data of the positron emitter nuclei of 7–20 min half-lives is not contributed for the analysis of decay curve if the information of the reaction cross section, the composition of a human body tissue, and the number of decay events in 200 s are considered. Therefore, it was approximated by Eq. (1)

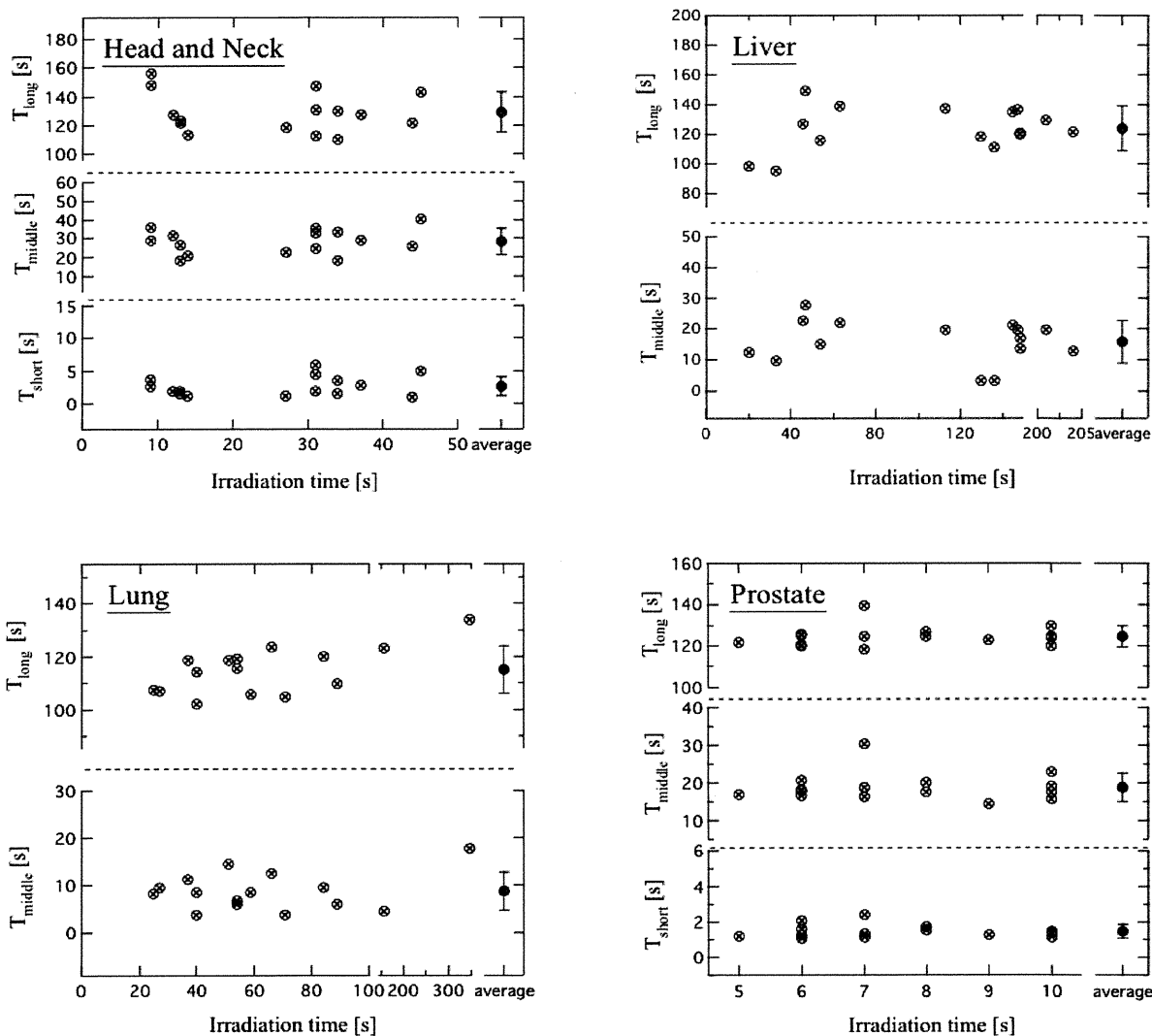


FIG. 6. The distribution of the three half-life values relative to irradiation time at each treatment site.

using three elements, which were half-lives from 1 s to 1–2 min. It was assumed that the nuclei with a few minutes half-lives such as ^{14}O and ^{15}O were attributed to T_{long} , the nuclei with several seconds half-lives including ^{10}C to T_{middle} and the nuclei with few seconds half-lives such as ^{38}Ca and ^{39}O to T_{short}

$$N(t) = F(A) \cdot \left(\frac{1}{2}\right)^{t/T_{\text{long}}} + F(B) \cdot \left(\frac{1}{2}\right)^{t/T_{\text{middle}}} + F(C) \cdot \left(\frac{1}{2}\right)^{t/T_{\text{short}}} \quad (1)$$

Here, t is measured time of activity, T_{long} , T_{middle} , and T_{short} are half-life values, and $F(A)$, $F(B)$, and $F(C)$ are the activity after proton irradiation relative to each half-life value. The intensity of the activity of short half-life decreases by increasing of the irradiation time. The quantity of the decreased activity will be estimated using the decay correction of the activity during proton irradiation. However, the mea-

sured activity in the case of the actual proton treatment time is important for activity simulation in patient body. Therefore, in this manuscript, the quantity of activity after proton irradiated in clinical therapy was verified. The decay curves of the measured activity include a washout effect of each organ, quantities and kinds of positron emitter nuclei generated in a patient body by proton irradiation.

Figure 6 shows the distribution of the three half-life values determined based on a fit to the measured data relative to irradiation time at each site by use of fitting calculation with the software of IGOR pro 6.1 (WaveMetrics, USA). The fitting results are summarized in Table IV. The values of T_{long} , T_{middle} , and T_{short} were about 115–130, 8–30, and 1–3 s. T_{long} and T_{middle} are mixed value of the half-life value of ^{10}C , ^{11}C , ^{13}N , ^{14}O , ^{15}O , and ^{38}K , and T_{short} is mixed value of the half-life value of ^{38}Ca and ^{39}Ca . Furthermore, the main component of T_{long} is the half-life value of ^{15}O and the main component of T_{middle} is the half-life value of ^{10}C . The time of

TABLE IV. Three ratios of number and half-life values of measured activity at each treatment site.

Site	$F(A)/N(0)(\pm\Delta(F(A)/N(0)))$	$T_{\text{long}}(\pm\Delta T_{\text{long}})$ (s)	$\Delta(F(A)/N(0))/(F(A)/N(0))$ (%)	$\Delta T_{\text{long}}/T_{\text{long}}$ (%)
Head and neck	0.538(\pm 0.0662)	129(\pm 14.1)	12.3	10.9
Liver	0.679(\pm 0.0732)	124(\pm 15.0)	10.8	12.1
Lung	0.778(\pm 0.0592)	115(\pm 8.79)	7.60	7.65
Prostate	0.408(\pm 0.0306)	125(\pm 5.11)	7.50	4.10
Site	$F(B)/N(0)(\pm\Delta(F(B)/N(0)))$	$T_{\text{middle}}(\pm\Delta T_{\text{middle}})$ (s)	$\Delta(F(B)/N(0))/(F(B)/N(0))$ (%)	$\Delta T_{\text{middle}}/T_{\text{middle}}$ (%)
Head and neck	0.272(\pm 0.0527)	28.2(\pm 6.72)	19.3	23.9
Liver	0.321(\pm 0.0732)	16.1(\pm 6.98)	22.8	43.5
Lung	0.222(\pm 0.0592)	8.73(\pm 4.00)	26.7	45.8
Prostate	0.223(\pm 0.0286)	18.8(\pm 3.80)	12.9	20.2
Site	$F(C)/N(0)(\pm\Delta(F(C)/N(0)))$	$T_{\text{short}}(\pm\Delta T_{\text{short}})$ (s)	$\Delta(F(C)/N(0))/(F(C)/N(0))$ (%)	$\Delta T_{\text{short}}/T_{\text{short}}$ (%)
Head and neck	0.190(\pm 0.0739)	2.61(\pm 1.52)	38.9	58.3
Liver	—	—	—	—
Lung	—	—	—	—
Prostate	0.369(\pm 0.0503)	1.46(\pm 0.366)	13.6	25.0

proton irradiation is long for method of gating irradiation in treatment of the liver and lung tumor. Moreover, the volume of the bone that contains a lot of ^{40}Ca nuclei in the irradiated area is small. Therefore, the decay curves were approximated with two half-life values of T_{long} and T_{middle} in the liver and lung. In the head and neck and prostate, the decay curve was estimated using all three elements. The value of $\Delta T_{\text{long}}/T_{\text{long}}$ was about 10% and T_{middle} and T_{short} were in the range of 20%–60%. The three half-life values that were determined based on a fit to the measured data did not depend on irradiation time greatly.

On the other hand, the parameters of $F(A)$, $F(B)$, and $F(C)$ were related to irradiation time. The precision of $F(A)$ was about 10%, $F(B)$ and $F(C)$ were 10%–40%. While the number of positron emitter nuclei generated in a patient's body increases with the amount of proton irradiation, it declines according to the half-life value during proton irradiation. The detected number of the activity data of nuclei with short half-lives decreases in long time of proton irradiation. Therefore, the contribution of the measured activity data of short half-life is less for analysis of the decay curve fitting and the accuracy of $F(A)$ of activity decay curve of nuclei with long half-lives has improved as the results.

There are some research reports of a study for activity decay curves of the positron emitter nuclei generated in a human body by proton irradiation. The decay curves include half-lives and washout of the generated positron emitter nuclei. Parodi *et al.*¹³ (2007) performed measurement and simulation of patient's decay curves observed by beam off-line PET type and calculation results of the activity decay curves using human composition data by ICRU (Ref. 16) was reported by our study (2008).¹⁴ It was confirmed to approximate the activity decay curves of two or three elements

with a short, middle, and long half-life value from results of the verification data in beam off-line and on-line PET types.

Figure 7 shows parameters of $F(A)/N(0)$, $F(B)/N(0)$, and $F(C)/N(0)$, which are ratios of element each half-life value when a measurement time is 0 s in Eq. (1) to the irradiation time in treatment sites and patients, respectively. The parameters were formed by groups of each patient (color markers shown in Fig. 7) in all treatment sites. Therefore, it was guessed that the ratios of element in each half-life value to the irradiation time have dependence of individual patient in addition to a composition of body tissues in proton irradiated volume. In proton treatment of prostate, direction and number (two irradiated field) of irradiated field, and organ such as the skin, the muscle, the thighbone, and prostate in the irradiated volume are the same in all the patients. Therefore, the main difference of the parameter in case of prostate was shown by an individual patient. The precision of the ratios of element each half-life value in prostate was 4% in $F(A)/N(0)$, 7% in $F(B)/N(0)$, and 7% in $F(C)/N(0)$. The parameter obtained by activity measured from each patient in our work will be useful for the simulation of activity distribution in a human body based on ICRU and NNDC data.

The results of the precisions of the half-life values and the activity after proton irradiation are relative to which the half-life value in the three elements. The quantities of the activity indicated that the stability of the value of T_{long} is high because of small dispersion of detected number of activity with long half-lives in measurement time of 200 s. The generated ^{15}O nuclei were important for activity imaging of the proton irradiated volume in a patient. The positron emitter nuclei of half-life values of T_{middle} and T_{short} may be used for the statistical increase and the time dependence correction of detected activity events in a proton scanning or a gating irra-

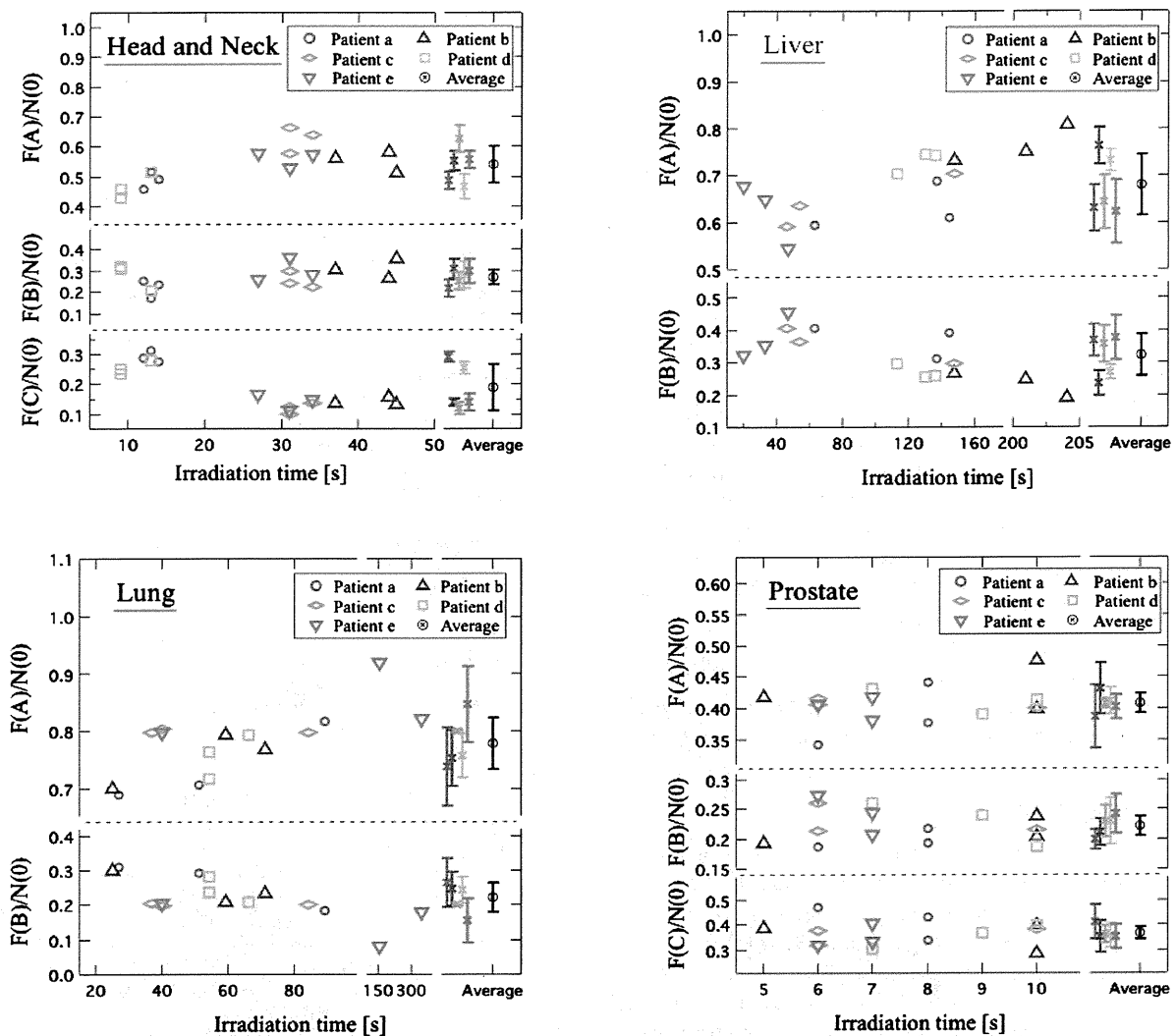


FIG. 7. The values of $F(A)/N(0)$, $F(B)/N(0)$ and $F(C)/N(0)$ to irradiation time of head and neck, liver, lung, and prostate patients, respectively. The color of the marker shows individual patient. Each error bar of a color marker shows a standard deviation of each ratio in the same patient. An error bar of a black marker shows an average ratio and standard deviation in patients of the same treatment site.

diation with the time structure. But now, the development of the software to measure activity during beam-off in synchronized irradiation method with high precision is inadequate.

The differences in these values were caused by the different kinds of positron emitter nuclei generated according to the irradiation time and the composition of the tissue. From the reactions involving ^{12}C and ^{16}O , positron emitter nuclei such as ^{11}C , ^{13}N , ^{14}O , and ^{15}O are generated, the half-life values of which are several minutes long, as is ^{10}C , which has a half-life value of 20 s. Moreover, ^{39}Ca (half-life value: 859.6 ms), ^{38}Ca (half-life value: 447 ms), and ^{38}K (half-life value: 7.63 min) are generated from target nuclear fragment reactions between proton nuclei and Ca nuclei, which are the main component of bones such as cranial bones, ribs, and the femur. As the irradiated volume includes much bone tissue especially in the head and neck and prostate, it is necessary to take the positron emitter nuclei generated from Ca nuclei into consideration. The ranges of the half-life values in the

prostate were smaller than in the head and neck. In the head and neck, the proton beam is irradiated in various places. So, the irradiation conditions such as irradiation field, irradiation direction, and the number of ports varies greatly from patient to patient. In other words, the tissue in the irradiated volume differs in each patient. For example, the irradiated volume may include the temporomandibular joint, cheek bone, paranasal sinuses, and so on. On the other hand, in the prostate, because the irradiation time is short and the position of the target and the irradiation conditions are almost predefined, there is little difference in each patient's irradiation conditions. So for the prostate, the three elements' half-life values can be approximated with high precision and the ranges of these values were smallest.

The ratio of the $F(A)/N(0)$ was range of 0.408–0.778 and was larger than the ratios of $F(B)/N(0)$ and $F(C)/N(0)$. The ratios were small and were in the range of 0.190–0.369. The A-activity half-life value of about 2 min was equivalent in

that of ^{15}O . Almost all positron emitter nuclei generated by target nuclear fragment reactions in a human body are estimated to be ^{15}O by considering the composition of a human body tissue (Table I), the reaction channel (Table II), and the reaction cross section (Fig. 2). Therefore, the detection of ^{15}O is important for monitoring the proton irradiated volume. The proton beam irradiation time should be short for much detection of ^{15}O because the ^{15}O decreases during the proton beam irradiation. Furthermore, the number of generated positron emitter nuclei in which ^{15}O is the main component relative to the irradiation dose can be ascertained by using the decay curves of measured activity. Also, the information of the measured decay curve in each treatment site will be of importance for the proton scanning method with the time dependence at the irradiation position rather than the passive irradiation method likely to the double scattering method. There are some manuscripts about the application of on-line PET therapy monitoring for carbon raster scanning method.^{24,25} Spot scanning irradiation method or synchronized irradiation method has an interval of beam off. Therefore, activity data of the nuclei with short half-lives such as a few seconds are necessary and important for use of activity measured in the interval. These data can then be used to surmise the irradiated dose the patient received. *In vivo* dosimetry is therefore expected to be realized in the future.

IV. CONCLUSION

We verified the features of the activity of positron emitter nuclei generated in a patient body by using BOLPs-RGp. The decay curves which are measured activity by BOLPs-RGp including both a quantity and kind of positron emitter nuclei generated by proton irradiation in a patient body and washout effect in each organ or tissue can be approximated with two or three half-life values in the four treatment sites of head and neck, liver, lung, and prostate. For the monitoring of the proton irradiated volume and the *in vivo* dosimetry, the importance of ^{15}O generated in a human body was entirely new confirmation by the clinical data measured by BOLPs-RGp.

This report demonstrated the kinds of positron emitter nuclei generated in a patient's body during proton therapy and may be the first do this. The data of decay curves of the measured activity in proton treatment are utilized for the verification of activity distribution simulation using Monte Carlo method and other calculation methods. For the purpose of completing the simulation system, the data can be utilized to verify the difference between the dose distribution of the calculated treatment plan and the activity distribution calculated by the simulation system using data from the patient's body. Furthermore, the realization of *in vivo* dosimetry can be expected by using these data to acquire with high accuracy a value for the amount of activity generated relative to the amount of proton irradiation dose. These data are also important as well as the verification data of radionuclide source measurements and phantom irradiations for verifying the validity of the specification of the BOLPs-RGp and for increasing its precision.

ACKNOWLEDGMENTS

The authors would like to thank T. Okamoto of Hamamatsu Photonics K. K., H. Oka, and K. Tojima of SGI Japan, Ltd. for technical support. The authors also acknowledge the staff members of the Proton Radiotherapy Department of National Cancer Center, Kashiwa for help and the members of SHI Accelerator Service Ltd. and Accelerator Engineering Inc. for the operation of the proton apparatus. This work was supported by Health and Labor Science Research Grants from the Japanese Government.

¹Electronic mail: aya_miyatake@tr-corp.jp

²<http://ptcog.web.psi.ch/Archive/Patientstatistics-update02Mar2009.pdf>

³U. Oelfke, G. Lam, and M. Atkins, "Proton dose monitoring with PET: Quantitative studies in Lucite," *Phys. Med. Biol.* **41**, 177–196 (1996).

⁴D. W. Litzenberg, D. A. Roberts, M. Y. Lee, K. Pham, A. M. Vander Molen, R. Ronningen, and F. D. Bechetti, "On-line monitoring of radiotherapy beams: Experimental results with proton beams," *Med. Phys.* **26**(6), 992–1006 (1999).

⁵K. Parodi and W. Enghardt, "Potential application of PET in quality assurance of proton therapy," *Phys. Med. Biol.* **45**, N151–N156 (2000).

⁶T. Nishio, T. Ogino, M. Shimbo, S. Katsuta, S. Kawasaki, T. Murakami, T. Sato, Y. Kojima, K. Murakami, and H. Ikeda, "Distributions of β^+ decayed nucleus produced from the target fragment reaction in $(\text{CH}_2)_n$ and patient liver targets by using a proton beam for therapy," in Abstracts of the XXXIV PTCOG Meeting, Boston, MA, 2001, pp. 15–16.

⁷K. Parodi, W. Enghardt, and T. Haberer, "In-beam PET measurements of β^+ radioactivity induced by proton beams," *Phys. Med. Biol.* **47**, 21–36 (2002).

⁸Y. Hishikawa, K. Kagawa, M. Murakami, H. Sasaki, T. Akagi, and M. Abe, "Usefulness of positron-emission tomographic images after proton therapy," *Int. J. Radiat. Oncol. Biol. Phys.* **53**, 1388–1391 (2002).

⁹W. Enghardt, P. Crespo, F. Fiedler, R. Hinz, K. Parodi, J. Pawelke, and F. Ponisch, "Dose quantification from in-beam positron emission tomography," *Radiother. Oncol.* **73**, S96–S98 (2004).

¹⁰T. Nishio, T. Sato, H. Kitamura, K. Murakami, and T. Ogino, "Distributions of β^+ decayed nuclei generated in the CH_2 and H_2O targets by the target nuclear fragment reaction using therapeutic MONO and SOBP proton beam," *Med. Phys.* **32**(4), 1070–1082 (2005).

¹¹K. Parodi, F. Ponisch, and W. Enghardt, "Experimental study on the feasibility of in-beam PET for accurate monitoring of proton therapy," *IEEE Trans. Nucl. Sci.* **52**, 778–786 (2005).

¹²T. Nishio, T. Ogino, K. Nomura, and H. Uchida, "Dose-volume delivery guided proton therapy using beam on-line PET system," *Med. Phys.* **33**(11), 4190–4197 (2006).

¹³K. Parodi, H. Paganetti, E. Cascio, J. B. Flanz, A. A. Bonab, N. M. Alpert, K. Lohmann, and T. Bortfeld, "PET/CT imaging for treatment verification after proton therapy: A study with plastic phantoms and metallic implants," *Med. Phys.* **34**(2), 419–435 (2007).

¹⁴K. Parodi, H. Paganetti, H. A. Shih, S. Michaud, J. S. Loeffler, T. F. Delaney, N. J. Liebsch, J. E. Munzenrider, A. J. Fischman, A. Knopf, and T. Bortfeld, "Patient study of in vivo verification of beam delivery and range, using positron emission tomography and computed tomography imaging after proton therapy," *Int. J. Radiat. Oncol. Biol. Phys.* **68**(3), 920–934 (2007).

¹⁵T. Nishio, A. Miyatake, K. Inoue, S. Katsuta, T. Gomi-Miyagishi, R. Kohno, S. Kameoka, K. Nakagawa, and T. Ogino, "Experimental verification of proton beam monitoring in a human body by use of activity image of positron-emitting nuclei generated by nuclear fragmentation reaction," *Radiol. Phys. Technol.* **1**(1), 44–54 (2008).

¹⁶T. Nishio, A. Miyatake, T. Ogino, K. Nakagawa, N. Saijo, and H. Esumi, "The development and clinical use of a beam on-line PET system mounted on a rotating gantry port in proton therapy," *Int. J. Radiat. Oncol. Biol. Phys.* **76**(1), 277–286 (2010).

¹⁷ICRU, "Photon, electron, proton and neutron interaction data for body tissues," ICRU Report No. 46, 11–13 (1992).

¹⁸NNDC, <http://www.nndc.bnl.gov/>.

¹⁹H. Uchida, T. Okamoto, T. Ohmura, K. Shimizu, N. Satoh, T. Koike, and T. Yamashita, "A compact planar positron imaging system," *Nucl. In-*

- strum. Methods Phys. Res. A **516**, 564–574 (2004).
- ¹⁹T. Tomitani *et al.*, “Washout studies of ^{11}C in rabbit thigh muscle implanted by secondary beams of HIMAC,” *Phys. Med. Biol.* **48**, 875–889 (2003).
- ²⁰H. Mizuno *et al.*, “Washout measurement of radioisotope implanted by radioactive beams in the rabbit,” *Phys. Med. Biol.* **48**, 2269–2281 (2003).
- ²¹F. Fiedler *et al.*, “In-beam PET measurements of biological half-lives of ^{12}C irradiation induced β^+ -activity,” *Acta Oncol. (Madr)* **47**, 1077–1086 (2008).
- ²²W. L. Hughes, G. H. Nussbaum, R. Connolly, B. Emami, and P. Reilly, “Tissue perfusion rate determined from the decay of oxygen-15 activity after photon activation in situ,” *Science* **204**(4398), 1215–1217 (1979).
- ²³R. K. Ten Haken, G. H. Nussbaum, B. Emami, and W. L. Hughes, “Photon activation- ^{15}O decay studies of tumor blood flow,” *Med. Phys.* **8**, 324–336 (1981).
- ²⁴J. Pawelke, W. Enghardt, T. Haberer, B. G. Hasch, R. Hinz, M. Kramer, K. Lauckner, and M. Sobiella, “In-beam PET imaging for the control of heavy-ion tumour therapy,” *IEEE Trans. Nucl. Sci.* **44**, 1492–1498 (1997).
- ²⁵W. Enghardt, P. Crespo, F. Fiedler, R. Hinz, K. Parodi, J. Pawelke, and F. Pönisch, “Charged hadron tumour therapy monitoring by means of PET,” *Nucl. Instrum. Methods Phys. Res. A* **525**, 284–288 (2004).

Measurement of absorbed dose, quality factor, and dose equivalent in water phantom outside of the irradiation field in passive carbon-ion and proton radiotherapies

Shunsuke Yonai,²⁾ Yuki Kase, and Naruhiro Matsufuji
National Institute of Radiological Sciences, 4-9-1 Anagawa, Inage-ku, Chiba, Chiba 263-8555, Japan

Tatsuaki Kanai
Gunma University, 3-39-22 Showa-machi, Maebashi, Gunma 371-851, Japan

Teiji Nishio
National Cancer Center Hospital East, 6-5-1 Kashiwano-ha, Kashiwa, Chiba 277-8577, Japan

Masao Namba
Yokohama City University, 3-9 Fukuura, Kanazawa-ku, Yokohama, Kanagawa 236-0004, Japan

Wataru Yamashita
Tohoku University, Aramaki-Aza-Aoba, Aoba-ku, Sendai, Miyagi 980-8579, Japan

(Received 9 February 2010; revised 9 June 2010; accepted for publication 9 June 2010; published 13 July 2010)

Purpose: Successful results in carbon-ion and proton radiotherapies can extend patients' lives and thus present a treatment option for younger patients; however, the undesired exposure to normal tissues outside the treatment volume is a concern. Organ-specific information on the absorbed dose and the biological effectiveness in the patient is essential for assessing the risk, but experimental dose assessment has seldom been done. In this study, absorbed doses, quality factors, and dose equivalents in water phantom outside of the irradiation field were determined based on lineal energy distributions measured with a commercial tissue equivalent proportional counter (TEPC) at passive carbon-ion and proton radiotherapy facilities.

Methods: Measurements at eight positions in the water phantom were carried out at the Heavy-Ion Medical Accelerator in Chiba of the National Institute of Radiological Sciences for 400 and 290 MeV/u carbon beams and at the National Cancer Center Hospital East for a 235 MeV proton beam.

Results: The dose equivalent per treatment absorbed dose at the center of the range-modulated region H/D_t decreased as the position became farther from the beam axis and farther from the phantom surface. The values of H/D_t ranged from 6.7 to 0.16 mSv/Gy for the 400 MeV/u carbon beam, from 1.3 to 0.055 mSv/Gy for the 290 MeV/u carbon beam, and from 4.7 to 0.24 mSv/Gy for the 235 MeV proton beam. The values of the dose-averaged quality factor Q_D ranged from 2.4 to 4.6 for the 400 MeV/u beam, from 2.8 to 5.3 for the 290 MeV/u beam, and from 5.1 to 8.2 for the proton beam. The authors also observed differences in the distributions of H/D_t and Q_D between the carbon and proton beams.

Conclusions: The authors experimentally obtained absorbed doses, dose-averaged quality factors, and dose equivalents in water phantom outside of the irradiation field in passive carbon-ion and proton radiotherapies with TEPC. These data are very useful for estimating the risk of secondary cancer after receiving passive radiotherapies and for verifying Monte Carlo calculations. © 2010 American Association of Physicists in Medicine. [DOI: 10.1118/1.3458721]

Key words: carbon-ion radiotherapy, proton radiotherapy, dose equivalent, quality factor, tissue equivalent proportional counter

I. INTRODUCTION

In carbon-ion and proton radiotherapies, undesired radiation exposure in normal tissues around the treatment volume is less than that in conventional radiotherapies because of the definite beam range of the particles. Still, undesired exposure outside the treatment volume by secondary radiation has become a concern because successful results in carbon-ion and proton radiotherapies can extend patients' lives, and then the radiotherapies can become a treatment option for younger patients.¹⁻⁵ Such exposure is considerably lower than within

the treatment volume, but it is not negligible for estimating the risk of secondary cancer, especially for young patients. It is thus important to investigate the risk, including the contribution of secondary neutrons that are inevitably produced within the patient and beam line devices due to the potency of their biological effect.

Two methods for making a laterally uniform dose distribution are used in carbon-ion and proton radiotherapies at present: Passive and active methods. The passive method, which is known as the broad beam method, makes a laterally uniform broad field by double scattering or wobbling and

subsequently shapes the irradiation field by collimating the beam. The active method, on the other hand, shapes the irradiation field by scanning a pencil-like narrow beam without collimation. The active method can theoretically reduce the undesired dose in the normal tissue compared to the passive method because of the reduction of secondary neutrons produced within beam line devices such as a collimator.^{6–10} Also, the active method can theoretically improve the conformity in the target because of its flexibility for making an irradiation beam. However, the passive method will not be displaced anytime soon by the active one and may be used in combination with the active method in the future because the beam scanning technology has not yet been established for the treatment of moving targets.^{11,12} It is still important to provide accurate data essential to the risk assessment of a patient receiving carbon-ion or proton radiotherapy with the passive method.

Organ-specific information on the absorbed dose and biological effectiveness in the patient is essential for assessing the risk because neutrons are the main component of the undesired exposure and the undesired dose is not uniformly distributed in the human body.¹³ Additionally, the risks to different organs vary.¹⁴ Several papers have recently been published on risk assessment.^{2–5,15–17} Such investigations are often performed using Monte Carlo calculations. However, experimental assessments of dosimetric data in a phantom are scarce; thus, little experimental verification of the Monte Carlo calculation has been performed.

Mesoloras *et al.*¹⁸ evaluated the neutron dose equivalent to a representative point for a fetus of a mother receiving passive proton radiotherapy experimentally with a bubble detector and an anthropomorphic phantom. However, they used the average neutron quality factor based on the Monte Carlo calculation by Jiang *et al.*¹⁹ Wroe *et al.*^{20,21} measured the dose equivalent in passive proton fields for various clinical treatments with a silicon-on-insulator microdosimeter and an anthropomorphic phantom or a block phantom made of Lucite or polystyrene. They provided the dose equivalent and the average quality factor as a function of the depth in the phantom and the lateral distance from the beam edge.

In this study, lineal energy distributions in water phantom were measured using a commercial tissue equivalent proportional counter (TEPC) at passive carbon-ion and proton radiotherapy facilities: The Heavy-Ion Medical Accelerator in Chiba (HIMAC) of the National Institute of Radiological Sciences (NIRS) and the National Cancer Center Hospital East (NCCHE). A TEPC is a conventional tool for microdosimetry, but its spatial resolution is critically limited due to the detector size.^{22–24} Therefore, in this study, detailed measurements of the distribution close to the field edge were not carried out. Instead, measurements were carried out in a wide area within the water phantom. Based on the measured lineal energy distributions, we obtained absorbed doses, quality factors and, consequently, dose equivalents. These measurements were compared to measurements reported in a published paper.

II. MATERIALS AND METHODS

II.A. Dosimetry

II.A.1. TEPC

We used a commercial TEPC [LET 1/2, 0.5 in. TE proportional counter, Far West Technology, Inc., Goleta, CA] which is one of Rossi-type counters with a helix around a central electrode. The TEPC technique is conventional and established for microdosimetry and this type of TEPC has been used often for measurements of lineal energy distribution in various radiation fields.^{25–29} It is composed of a spherical cavity with a 12.7 mm diameter, a tissue-equivalent (TE) plastic wall 1.27 mm thick (Shonka type A150), and a thin aluminum shell that serves as a vacuum-tight housing. The outer diameter is 21 mm. The cavity is filled with a propane-based TE gas mixture (54.6% C₃H₈, 40.16% CO₂, and 5.26% N₂ by volume) at a pressure of 4.4 kPa to simulate a site size of 1 μm . In order to obtain lineal energy distributions in the wider range, a signal from TEPC was integrated with a preamplifier (ORTEC 142B) and the signal was then divided into three main amplifiers (ORTEC 572/671) (ORTEC, Oak Ridge, TN) with different gains. Finally, these signals were separately sent to each multichannel analyzer (ORTEC Easy-MCA) to measure the pulse height. An energy calibration was performed with a ²⁴⁴Cm α -particle source built into the counters to convert the pulse height to the corresponding lineal energy. The lowest measurable lineal energy was 0.2 keV/ μm in our experiment due to signal noise.

II.A.2. Determination of absorbed dose, quality factor, and dose equivalent

In this study, the absorbed dose D , dose equivalent H , and dose-averaged quality factor Q_D , were determined from the frequency distribution as a function of y [$f(y)$], the so-called lineal energy distribution, which can be obtained directly by the measurement with TEPC. A quality factor was introduced to weight the absorbed dose for the biological effectiveness of radiation at low exposure levels encountered in radiation-protection practices based on the ionization density of charged particles and an assumption about a shape of the dose-effect relationship for human risk at low doses.^{30,31} H , which is a product of Q and D , was defined for routine radiation-protection applications and should not be used in the numerical assessment of high exposure levels encountered in radiation accidents. The use of H is reasonable in this study because the dose measured in this study was expected to be categorized into the low dose level as in a previous study.⁶

The variable y is a stochastic quantity and is defined as the quotient of the energy imparted to matter in a given volume by a single event by the mean chord length l . The related quantity, the specific energy z , is defined as the quotient of the energy imparted to matter by one or more events by the mass. The mean values of y and z are microdosimetric analogs of linear energy transfer L and D , respectively.^{22,32}

TABLE I. Summary of the beam parameters used in this study.

Facility	Method for making a laterally uniform irradiation field	Diameter of laterally uniform irradiation field (mm)	Width of the SOBPs (mm)	Aperture size of the adjustable precollimator (mm ²)	Distance between the aperture and isocenter (mm)	Aperture size of the final collimator (mm ²)
HIMAC	Single-wobbling	100	60	78 × 70 (aluminum FLC ^a)	600	58 × 50 (iron MLC ^b)
NCCHE	Double-scattering	283	60	90 × 90 (brass FLC ^a)	300	50 × 50 (brass PC ^c)

^aFour-leaf collimator.^bMultileaf collimator.^cPatient-specific collimator.

D and H were determined from measured $f(y)$ as the following equations:

$$D(y) = \frac{K}{M_{\text{gas}}} \cdot l \cdot (y \cdot f(y)), \quad (1)$$

$$D = \int_{0.2}^{y_{\text{max}}} D(y) dy, \quad (2)$$

$$H = \int_{0.2}^{y_{\text{max}}} Q(y) \cdot D(y) dy, \quad (3)$$

where y is the lineal energy in units of keV μm^{-1} , l is the mean chord length in units of μm , which is defined by two-thirds of the site size, M_{gas} is the mass of the TE gas in units of kg, K is the conversion factor from keV to J ($=1.602 \times 10^{-16}$), y_{max} is the maximum y in the measurement, and $Q(y)$ is the quality factor as a function of y . Two $Q(y)$ - y relationships were used based on two recommendations: The ICRP 60 recommendation with Eq. (4) assuming that y is equal to L and the ICRU 40 recommendation with Eq. (5).^{30,33}

$$\begin{aligned} Q(L) &= 1 \quad (L < 10 \text{ keV } \mu\text{m}^{-1}) \\ &= 0.32L - 2.2 \quad (10 \leq L < 100 \text{ keV } \mu\text{m}^{-1}) \\ &= 300/\sqrt{L} \quad (L \geq 100 \text{ keV } \mu\text{m}^{-1}) \end{aligned} \quad (4)$$

$$\begin{aligned} Q(y) &= \frac{a_1}{y} [1 - \exp(-a_2 y^2 - a_3 y^3)], \\ a_1 &= 5510 \text{ keV } \mu\text{m}^{-1}, \\ a_2 &= 5 \times 10^{-5} \mu\text{m}^2 \text{ keV}^{-2}, \\ a_3 &= 2 \times 10^{-7} \mu\text{m}^3 \text{ keV}^{-3}. \end{aligned} \quad (5)$$

Folkerts *et al.*³⁴ implied that $Q(y)$ in the neutron and photon mixed field calculated by these equations are significantly different. The dose-averaged quality factor Q_D can be obtained from the following equation:

$$Q_D = \int Q(y) \cdot D(y) dy / \int D(y) dy. \quad (6)$$

Finally, D and H were normalized by the treatment absorbed dose at the center of the range-modulated region D_r .

II.B. Experimental setup

Measurements were performed using the horizontal beam line in treatment room B at HIMAC for the carbon beam and the gantry beam line at NCCHE for the proton beam. The beam energies used in this study were 290 and 400 MeV/u for the carbon beam and 235 MeV for the proton beam. 400 MeV/u and 235 MeV are the maximum beam energy used in radiotherapy at each facility. These energies were defined as the energies of the ions when extracted from the accelerator. It is essential for an event-by-event measurement of an energy deposition to avoid pile-up events. Since the number of the TEPC signal varies significantly at the measured position, the beam intensity was adjusted at each measurement and reduced by approximately 0.1–0.001 compared to that at the treatment (the adjustment values 0.1 and 0.001 were used at measurements at the positions farthest from the beam axis for the 290 MeV/u carbon beam and closest to the beam axis for the 400 MeV/u carbon beam, respectively).

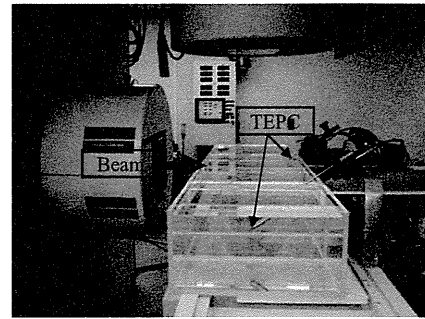
The published papers show that the dose by secondary neutrons, which are the primary component in the total secondary dose outside of the irradiation field, depends strongly on the parameters of the beam-shaping devices.^{6,18,35–37} The parameters in this study were selected to follow those of the previous study.⁶ Table I summarizes the beam parameters used in this study. The width of the spread-out Bragg peak (SOBP) was set at 60 mm, which is the standard setting at HIMAC. A multileaf collimator (MLC) and patient-specific collimator were used as the final collimators at HIMAC and NCCHE, respectively. The aperture sizes of the final collimators were 58 × 50 and 50 × 50 mm² at HIMAC and NCCHE, respectively. This slight difference is due to the pitch size of the MLC at HIMAC. The diameters of the laterally uniform irradiation field were set at the values usually used in treatment at the individual facility: 100 mm at HIMAC and 283 mm at NCCHE. (At HIMAC, the diameter is selectable from 100, 150, and 200 mm according to the aperture size of the final collimator. The influence on the neutron dose was investigated in the previous study.⁶ The neutron dose increases 1.3 to 1.7 times when the diameter changes from 100 to 200 mm.) There is a difference in the

different sites' methods of ensuring a laterally uniform irradiation field: The single-wobbling method at HIMAC^{38,39} and the double-scattering method at NCCHE;⁴⁰ however, our previous study showed that the neutron dose does not depend on the method. Distances between the aperture and isocenter (I.C.) were set at the average values for treatment at the individual facility. The distance slightly influences the neutron dose. According to the previous study,⁶ the neutron dose decreases by about 10% when the distance changes from 500 to 700 mm for 290 and 400 MeV/u carbon beams, and the dose decreases by 5% to 20% when the distance changes from 300 to 500 mm for the 235 MeV proton beam. The beam ranges in water with parameters of beam-shaping devices used in this study are 253.6 and 146.8 mm for the 400 and 290 MeV/u carbon beams, and 261.6 mm for the proton beam. (The value at HIMAC was defined as the depth of the distal 80% point of the Bragg peak, and that at HCCHE was defined as the depth of the distal 90% point of the plateau dose within the SOBP.) The clinical RBEs used in treatment with the parameters are 2.36, 2.41, and 1.1 for the 400 and 290 MeV/u carbon beams and the proton beam, respectively.

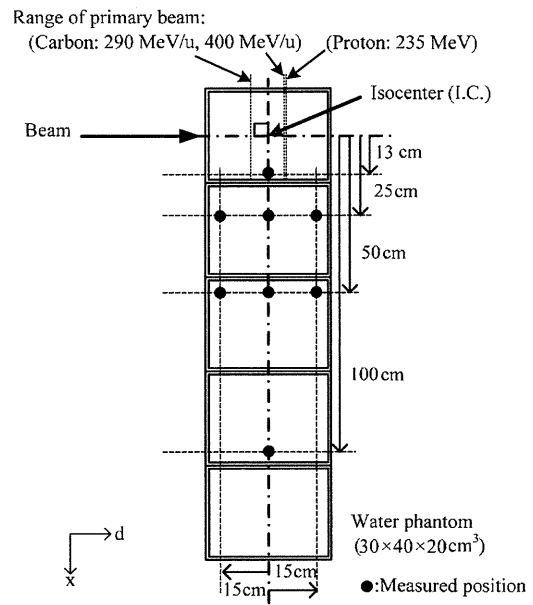
Figure 1 shows a photograph and schematic view of the experimental setup. The ranges of the primary beams are also shown in this figure. Five water phantoms with a 1 cm thick PMMA wall (external size, $30 \times 40 \times 20 \text{ cm}^3$; water-equivalent thickness of the wall, 1.16 cm) were placed to simulate a patient on a treatment bed. The center of the phantom coincided with the I.C. and the other four phantoms were lined up as shown in Fig. 1. The centers of all phantoms and the TEPC were set at the I.C. height. Measurements were carried out at eight positions for each incident beam. Here, we defined the coordinate system (x, d) in units of centimeters as shown in Fig. 1(b). The variable x is the off-axis distance and d is the depth in the water phantom (distance from the point on the phantom surface at which the initial beams enter, along the axis parallel to the beam axis). This means that I.C. is (0, 20) in the coordinate system. The four measured positions were on the I.C. line orthogonal to the beam axis and the distances from I.C. to the center of TEPC were 13, 25, 50, and 100 cm: (13, 20), (25, 20), (50, 20), and (100, 20). The other four positions were located 15 cm upstream/downstream of the I.C. line, and the distances from the beam axis were 25 and 50 cm: (25, 5), (50, 5), (25, 35), and (50, 35). As shown in Fig. 1(a), two TEPCs with the same property were employed to perform measurements at different positions in parallel.

III. RESULTS

Figures 2 and 3 show the measured D/D_t , H/D_t , and Q_D for the 400 and 290 MeV/u carbon beams, respectively. The difference in Q_D using the ICRU 40 and ICRP 60 recommendations was 5%–8% overall. The tendencies of D/D_t , H/D_t , and Q_D were the same for both energies of the carbon beam. D/D_t and H/D_t decreased as the position became farther from the beam axis (x increased) and farther from the phantom surface (d increased). In particular, D/D_t and H/D_t rapidly increased as x decreased for distances of $x \leq 50$ cm. The



a) Photograph of the experimental setup at HIMAC.



b) Schematic view of the experimental setup.

FIG. 1. Experimental setup. (a) Photograph of the experimental setup at HIMAC. (b) Schematic view of the experimental setup.

H/D_t value ranged from 6.7 to 0.16 mSv/Gy for the 400 MeV/u beam and from 1.3 to 0.055 mSv/Gy for the 290 MeV/u beam. Q_D decreased as the position became closer to the beam axis (x decreased), but did not depend on d . In the comparison between the 290 and 400 MeV/u carbon beams, D/D_t and H/D_t increased as the beam energy became higher; on the other hand, Q_D slightly increased as the beam energy became lower. The Q_D value ranged from 2.4 to 4.6 for the 400 MeV/u beam and from 2.8 to 5.3 for the 290 MeV/u beam.

Figure 4 shows the measured D/D_t , H/D_t , and Q_D for the 235 MeV proton beam. D/D_t and H/D_t for the proton beam depended on x and d as with the carbon beam, but did not increase rapidly as x became lower for distances of $x \leq 50$ cm unlike the carbon beam. The H/D_t value ranged from 4.7 to 0.24 mSv/Gy. Also, the tendencies of the Q_D distribution for the proton beam were different from the carbon beam. (1) The position where Q_D starts to drop was closer to the beam axis for the proton beam than for the